Neuron

Article

Neuronal mechanisms of nociceptive-evoked gamma-band oscillations in rodents

Graphical abstract

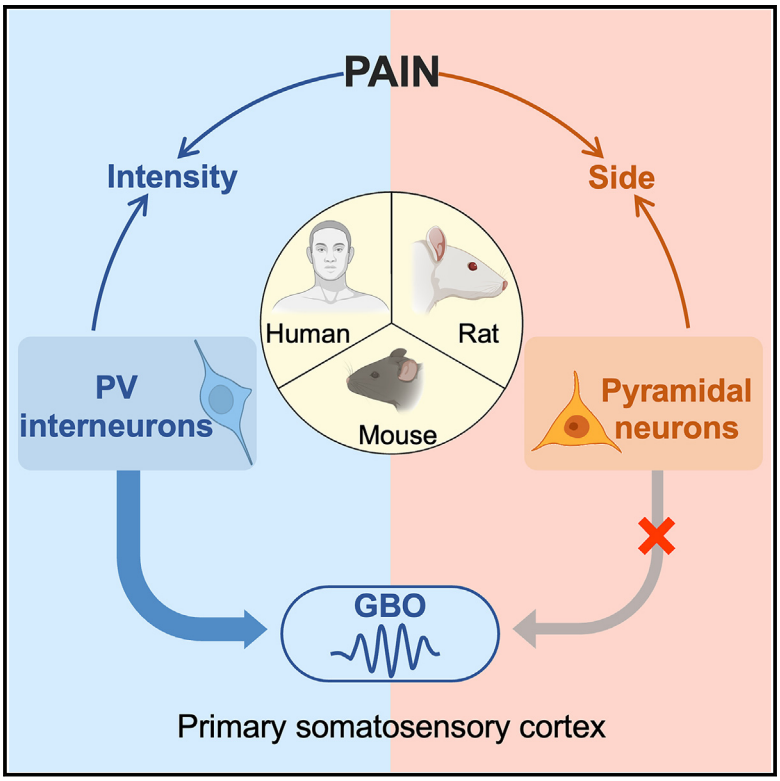

Authors

Lupeng Yue, Chongyu Bao, Libo Zhang, Fengrui Zhang, Wenqian Zhou, Gian Domenico Iannetti, Li Hu

Correspondence

huli@psych.ac.cn

In brief

Yue et al. investigate the neuronal mechanisms underlying nociceptive-evoked gamma-band oscillations (GBOs) in human and rodent models. Nociceptive-evoked GBOs preferentially encoding pain intensity are causally generated by parvalbumin (PV) interneurons in the primary somatosensory cortex. These findings provide valuable insights for developing targeted pain therapies aimed at modulating GBOs.

Highlights

- Nociceptive-evoked GBOs preferentially encode pain intensity across species
- Nociceptive-evoked GBOs in S1 are triggered by spiking of interneurons
- PV interneurons in S1 causally regulate behaviors for thermal and mechanical pains
- PV interneurons in S1 causally generate nociceptive-evoked GBOs

Yue et al., 2025, Neuron *113*, 769–784
March 5, 2025 © 2024 Elsevier Inc. All rights reserved, including those for text and data mining, AI training, and similar technologies.
https://doi.org/10.1016/j.neuron.2024.12.011

CellPress

Neuron

CellPress

Article

Neuronal mechanisms of nociceptive-evoked gamma-band oscillations in rodents

Lupeng Yue,[1,2,6] Chongyu Bao,[1,2,3,6] Libo Zhang,[1,2] Fengrui Zhang,[1,2] Wenqian Zhou,[1,2] Gian Domenico Iannetti,[4,5,7] and Li Hu[1,2,7,8,*]

[1]State Key Laboratory of Cognitive Science and Mental Health, Institute of Psychology, Chinese Academy of Sciences, Beijing, China
[2]Department of Psychology, University of Chinese Academy of Sciences, Beijing, China
[3]Center for Excellence in Brain Science and Intelligence Technology, Chinese Academy of Sciences, Shanghai, China
[4]Neuroscience and Behaviour Laboratory, Italian Institute of Technology, Rome, Italy
[5]Department of Neuroscience, Physiology, and Pharmacology, University College London, London, UK
[6]These authors contributed equally
[7]Senior author
[8]Lead contact
*Correspondence: huli@psych.ac.cn
https://doi.org/10.1016/j.neuron.2024.12.011

SUMMARY

Gamma-band oscillations (GBOs) in the primary somatosensory cortex (S1) play key roles in nociceptive processing. Yet, one crucial question remains unaddressed: what neuronal mechanisms underlie nociceptive-evoked GBOs? Here, we addressed this question using a range of somatosensory stimuli (nociceptive and non-nociceptive), neural recording techniques (electroencephalography in humans and silicon probes and calcium imaging in rodents), and optogenetics (alone or simultaneously with electrophysiology in mice). We found that (1) GBOs encoded pain intensity independent of stimulus intensity in humans, (2) GBOs in S1 encoded pain intensity and were triggered by spiking of S1 interneurons, (3) parvalbumin (PV)-positive interneurons preferentially tracked pain intensity, and critically, (4) PV S1 interneurons causally modulated GBOs and pain-related behaviors for both thermal and mechanical pain. These findings provide causal evidence that nociceptive-evoked GBOs preferentially encoding pain intensity are generated by PV interneurons in S1, thereby laying a solid foundation for developing GBO-based targeted pain therapies.

INTRODUCTION

The ability to identify noxious environmental events causing pain is pervasive in the animal kingdom, as it allows animals to avoid or reduce bodily injury and recover after it.[1,2] Pain, however, can also be maladaptive when it persists after healing, leading to unnecessary suffering and enormous economic costs.[3] To develop effective treatments and reduce suffering, it is crucial to understand how nociceptive inputs are processed in the nervous system to give rise to painful percepts.[3,4] Cortical oscillations in the gamma frequency (gamma-band oscillations, GBOs) evoked by nociceptive stimuli are increasingly investigated given their close relationship with nociceptive input across species,[5–7] which suggests that they may underpin pain perception. For this reason, they are a candidate target for therapeutic strategies, such as closed-loop brain-machine interfaces.[8] Nevertheless, one crucial mechanistic question remains to be fully addressed: what are the neuronal mechanisms underlying nociceptive-evoked GBOs? In this article, we provide a conclusive answer to this question.

This is a timely issue for two main reasons. First, previous human studies have yielded conflicting results about the relationship between nociceptive-evoked GBOs and pain. It has been suggested that GBOs are involved in various aspects of pain processing, such as encoding nociceptive stimulus intensity,[9–11] subjective pain intensity,[5,6,12] pain affect,[13] motor responses to pain,[14,15] and predictive error coding of pain.[9,16] Some studies even found a dissociation between GBOs and pain intensity.[17] These mixed findings might be associated with the fact that GBOs measured from the human scalp typically exhibit a low signal-to-noise ratio, particularly in studies with small sample sizes.[17] Second, the detailed investigation of the cellular substrates of GBOs has primarily focused on "spontaneous" rather than nociceptive-"evoked" oscillations. We previously suggested that nociceptive-evoked GBOs originate from interneurons in the primary somatosensory cortex (S1) contralateral to nociceptive stimulation.[18] Others have demonstrated that, within S1, parvalbumin (PV)-positive GABAergic interneurons are implicated in the generation of spontaneous GBOs. [7,19] However, no unequivocal evidence is available regarding the causal roles of PV interneurons in determining GBOs evoked by nociceptive stimuli. The distinction between spontaneous GBOs and evoked GBOs is crucial, as they are phenomenologically different and have different relationships with pain perception.[20]

All rights are reserved, including those for text and data mining, AI training, and similar technologies.

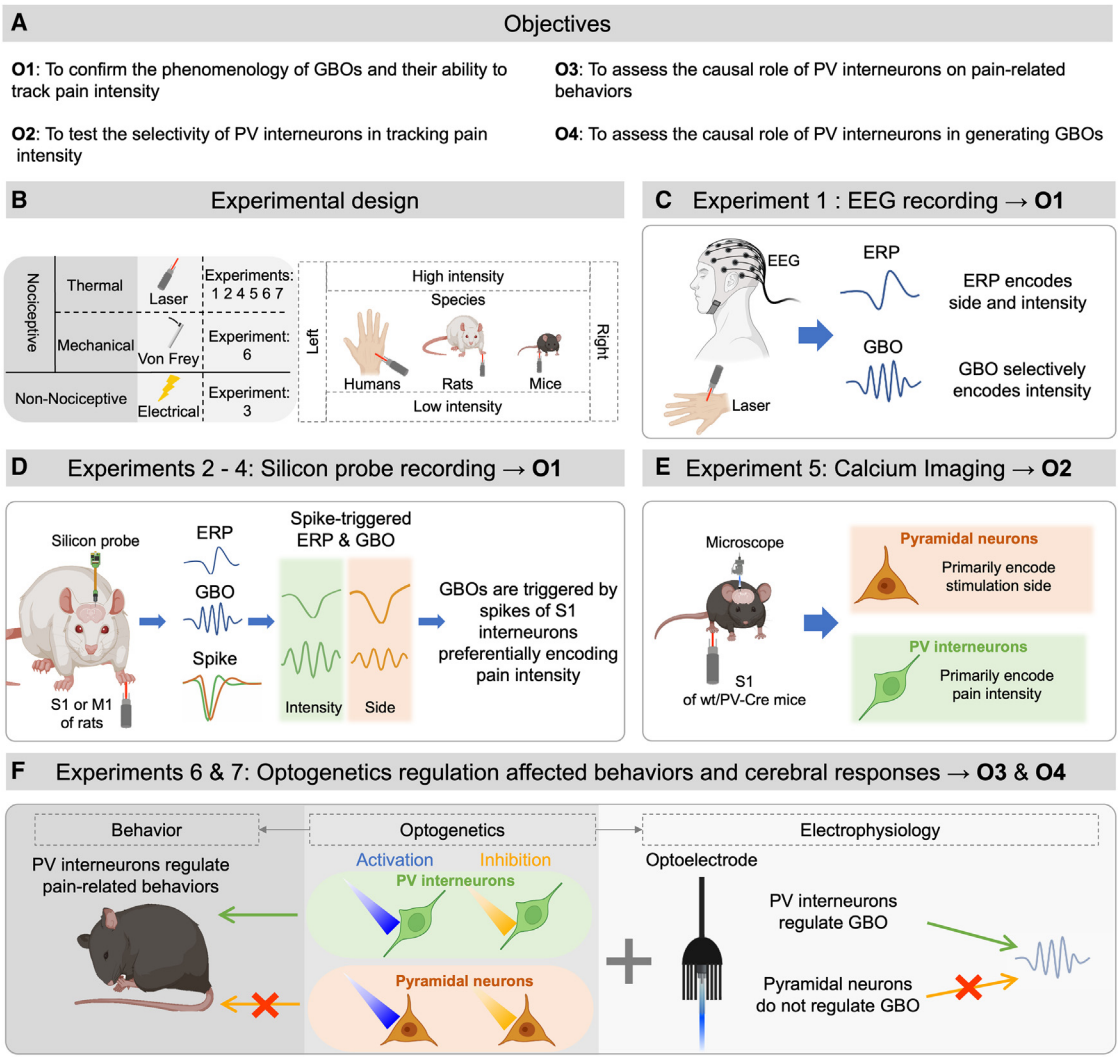

Figure 1. Research objectives and design

(A) This across-species study aimed to achieve four main objectives in seven experiments.

(B) We applied nociceptive (laser and mechanical) and non-nociceptive (electrical) stimuli in seven experiments (experiments 1, 2, 4, 5, 6, and 7: laser stimuli; experiment 3: electrical stimuli; experiment 6: mechanical stimuli). Stimuli of varying intensities were delivered to the right or the left side (paws or hands).

(C) 64-channel EEG was collected from 95 healthy human volunteers (experiment 1).

(D) High-density electrophysiological signals were collected from 20 freely moving rats using silicon probes implanted in S1 (experiments 2 and 3) or M1 (experiment 4).

(E) Calcium imaging data were collected from S1 of freely moving mice (experiment 5: 144 Pyr neurons from 5 WT mice and 122 PV interneurons from 3 PV-Cre mice).

(F) We used optogenetics to manipulate the activity of Pyr neurons and PV interneurons and thereby explore their causal relationship with pain-related behaviors and GBOs (experiments 6 and 7, n = 8–10 for ChR2 and NpHR in WT mice and PV-Cre mice).

This figure was created with BioRender.com.

To address the issue of the neuronal mechanisms underlying nociceptive-evoked GBOs and, therefore, to lay a solid foundation for the use of GBOs in pain research and clinical applications, we conducted seven across-species experiments combining a range of sensory stimuli (nociceptive and non-nociceptive); neural recording techniques (high-density electroencephalography [EEG] in humans and silicon probes and calcium imaging in rodents); and optogenetics (both alone and simultaneously with electrophysiology in mice) (Figure 1). We first used high-density EEG recordings to confirm the phenomenology of GBOs and test their ability to encode pain intensity in a large number of human participants (experiment 1). We then used silicon probes in rats to test whether GBOs in S1 encode pain intensity and assess their relationship to the spiking of interneurons and pyramidal (Pyr) neurons (experiments 2, 3, and 4). Subsequently, we used calcium imaging in mice to test whether PV interneurons preferentially track pain intensity and to confirm that Pyr neurons do not (experiment 5). Finally, we

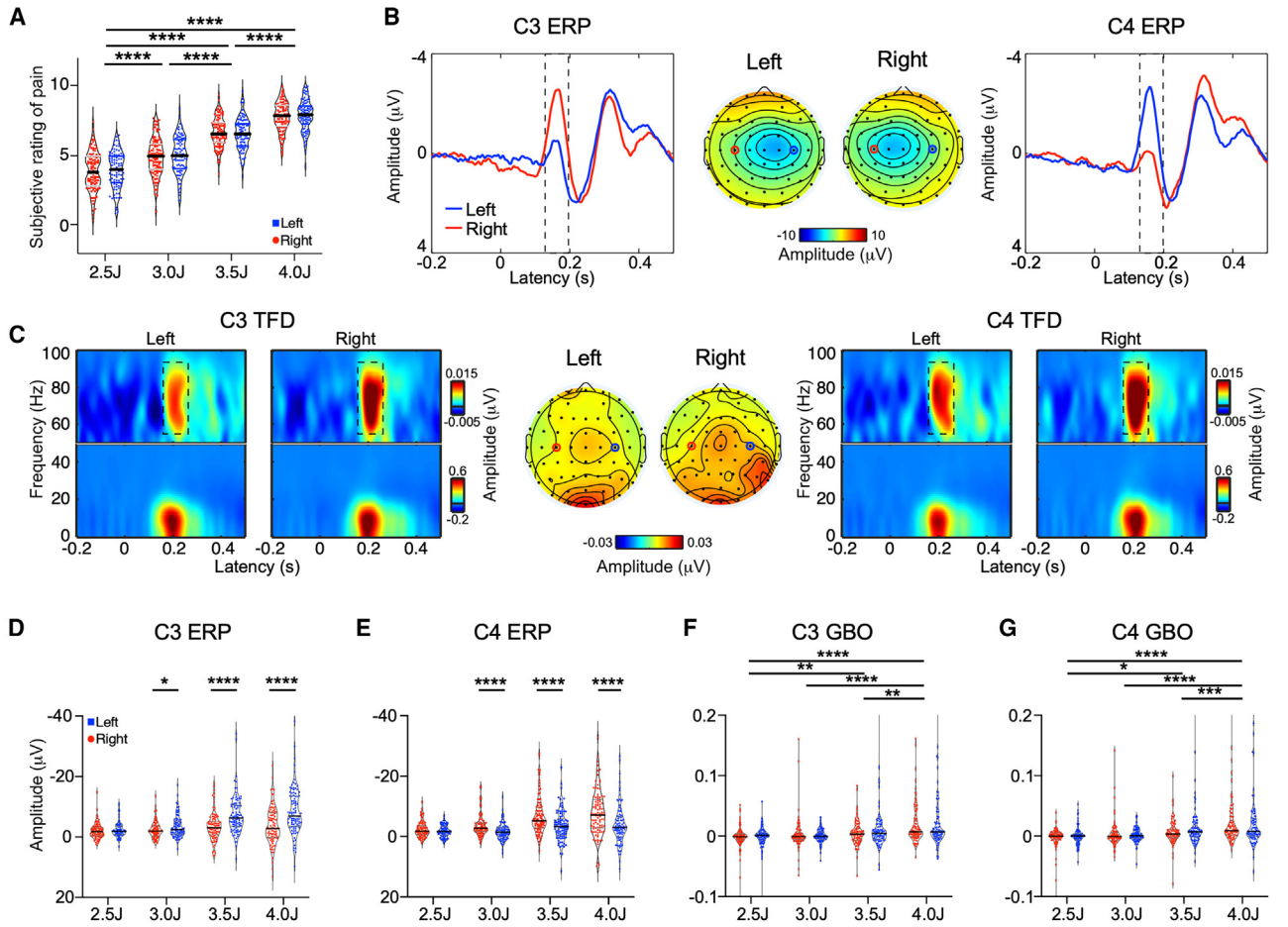

Figure 2. Nociceptive-evoked GBOs recorded from the human scalp-encoded stimulus intensity (experiment 1)

(A) Subjective ratings of pain were significantly modulated by stimulus intensity (****$p < 0.0001$, two-way repeated-measures ANOVA).

(B) ERP responses (1–30 Hz) at C3 (left, red circles) and C4 (right, blue circles) electrodes for left- and right-hand stimulation. The N1 wave showed a scalp topography with a negative maximum contralateral to the stimulated side.

(C) Time-frequency distributions (TFDs) of electrophysiological responses at C3 (left, red circles) and C4 (right, blue circles) electrodes for left- and right-hand stimulation. GBOs elicited by nociceptive stimuli (60–90 Hz, 150–250 ms) showed a centrally distributed scalp topography.

(D–G) Whereas N1 amplitudes were primarily modulated by stimulation side, especially at higher stimulus intensities (D and E), GBO magnitudes were only significantly modulated by pain intensity (F and G) (*$p < 0.05$, **$p < 0.01$, ***$p < 0.001$, ****$p < 0.0001$, two-way repeated-measures ANOVA with Bonferroni-corrected post hoc tests).

used optogenetics, both alone and combined with simultaneous electrophysiological recordings (optetrodes) in mice, to assess the causal role of the different classes of S1 neurons in generating nociceptive-evoked GBOs and pain-related behaviors (experiments 6 and 7).

RESULTS

Nociceptive-evoked GBOs in human EEG encode pain intensity (experiment 1)

We confirmed the phenomenology of nociceptive-evoked GBOs and their ability to track pain intensity in a large population of 95 healthy individuals (50 females, aged 21.6 ± 1.7 years [mean ± SD], range: 18–25 years). We coupled single-trial psychophysics with high-density EEG during laser stimulation of four intensity levels (Figures 1A–1C; see STAR Methods for experimental design). This radiant heat stimulation selectively excites cutaneous nociceptors and thereby elicits pure painful percepts without tactile sensations.[21,22]

Subjective ratings to laser stimulation of the left and right hands were clearly graded with stimulus intensity ($F(3,282) = 668.9$, $p < 0.0001$) but not dependent on stimulation side ($F(1,94) = 0.3699$, $p = 0.5445$; Figure 2A). GBOs elicited by nociceptive laser stimuli occurred at 150–250 ms post-stimulus, within a frequency range of 60–90 Hz. Their scalp topography showed a local maximum in the central region (Figure 2C). This topography confirms previous observations in independent samples of participants[23,24] and suggests that GBOs may originate from bilateral S1.[25] GBO amplitude measured from the electrodes above S1 (C3 or C4, circles in Figure 2C) was larger in trials with higher stimulus intensities (C3, $F(3,282) = 19.04$, $p < 0.001$; C4, $F(3,282) = 18.47$, $p < 0.001$) but independent of

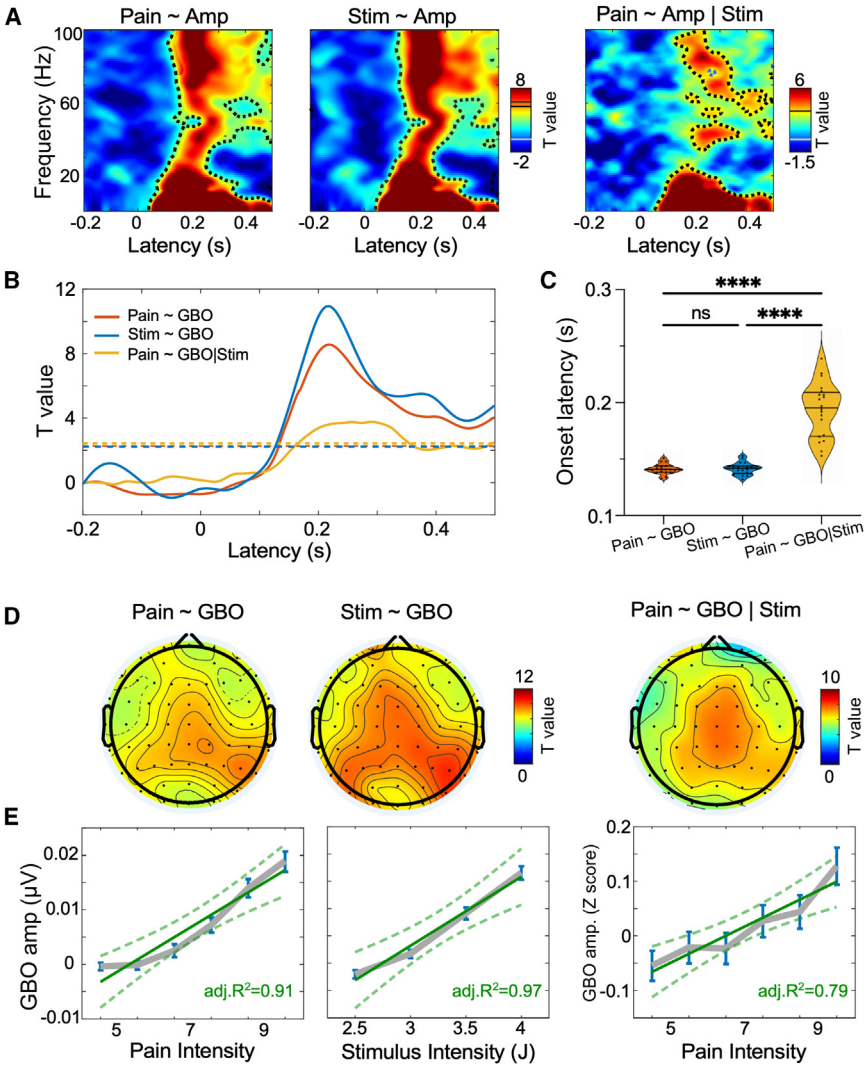

Figure 3. Nociceptive-evoked GBOs encoded pain intensity independent of stimulus intensity (experiment 1)

(A) Time-frequency distribution of the relationship between neural responses and (1) pain intensity (left), (2) stimulus intensity (middle), and (3) pain intensity independent of stimulus intensity (right). The LMM analyses were performed on neural responses collected at Cz electrode. Statistical t values are color-coded, and dotted curves enclose significant time-frequency regions with significant correlations.

(B) Time course of t values obtained from the LMM and averaged within the 50–100 Hz frequency range showing the dependence between GBO amplitudes and pain ratings (red), stimulus intensities (blue), and pain ratings after the effect of stimulus intensity was controlled for (yellow). Dashed lines represent significance thresholds (false discovery rate [FDR] corrected $p < 0.05$).

(C) Although the dependence between GBOs and both stimulus intensities and pain ratings had nearly identical onset latencies, the dependence between GBOs and pain ratings after stimulus intensity was controlled had a later onset latency (n.s., not significant, ****$p < 0.0001$; one-way repeated-measures ANOVA with Bonferroni-corrected post hoc tests).

(D) Scalp topographies of the relationship between GBO responses and pain intensity/stimulus intensity/pain intensity independent of stimulus intensity were all maximal at central electrodes.

(E) Linear fitting of the relationship between GBO amplitudes and pain intensity/stimulus intensity/pain intensity independent of stimulus intensity. Data were presented as mean ± SEM.

stimulation side (C3, $F(1,94) = 1.326$, $p = 0.2524$; C4, $F(1,94) = 0.7777$, $p = 0.3801$; Figures 2F and 2G). We also confirmed that nociceptive laser stimuli elicited large event-related potentials (ERPs), whose earliest component (i.e., the N1 wave peaking at 160 ms post-stimulus) displayed a negative maximum contralateral to the stimulated hand, compatible with a source in the corresponding S1[26] (Figure 2B). Although N1 peak amplitude was larger in trials with higher stimulus intensities (C3, $F(3,282) = 38.98$, $p < 0.0001$; C4, $F(3,282) = 34.47$, $p < 0.0001$; Figures 2D and 2E), this ERP-pain correlation has been repeatedly shown to be dependent on the saliency component of the stimulus.[12]

Next, we applied linear mixed models (LMMs) to single-trial data to examine the dose-response curve between (1) stimulus intensity and GBO amplitude, as well as (2) subjective rating and GBO amplitude.[27] Moreover, we assessed whether the relationship between subjective rating and GBO amplitude persisted independently of stimulus intensity by normalizing both subjective rating and GBO amplitude within each stimulus intensity with Z scores. LMM analyses revealed that both high-frequency GBOs and low-frequency ERPs were modulated by subjective rating and stimulus intensity (Figure 3A). Importantly, part of the amplitude of both responses reflected subjective rating independently of stimulus intensity, i.e., their relationship remained significant even after normalizing subjective ratings and GBO/ERP amplitudes within each stimulus intensity. While the dependence of GBOs on stimulus intensity and subjective rating occurred at nearly identical latencies ($p > 0.05$), the dependence of GBOs on pain rating after stimulus intensity was controlled occurred later (p values < 0.0001; Figures 3B and 3C). The observation that the correlation between GBO amplitude and subjective rating was maximal in central regions (Figure 3D) further suggests that GBOs may originate from bilateral S1.[25] This scalp topography also suggests that GBOs were unlikely to be caused by movement of the ears and other head muscles. Moreover, we observed that the relationship between GBO amplitude and stimulus intensity or subjective rating was well described using a linear model (GBO amplitude and stimulus intensity: adjusted $R^2 = 0.97$; GBO amplitude and subjective rating: adjusted $R^2 = 0.91$), even after controlling for stimulus intensity (adjusted $R^2 = 0.79$; Figure 3E). After characterizing the phenomenology of nociceptive-evoked GBOs in humans, we aimed to unravel their underlying neural mechanisms in rodents.

Nociceptive-evoked GBOs are triggered by spikes of S1 interneurons rather than those of Pyr neurons (experiments 2–4)

In experiment 2, we delivered nociceptive laser stimuli of two intensities (low and high) to the left and right forepaws of 14 adult male rats (Figure 1B; see STAR Methods for experimental design). We used video-based analysis to measure pain behavior and silicon probes to measure local field potentials (LFPs) and single-unit activity in the right S1 (Figures 1D, S1A, and S1B).

Nocifensive behaviors evoked by laser stimuli were significantly modulated by stimulus intensity ($F(1,13) = 75.62$, $p < 0.0001$), but not by stimulation side ($F(1,13) = 3.267$, $p = 0.094$), and there was no interaction between these factors ($F(1,13) = 1.002$, $p = 0.34$; Figure 4A).

From LFPs, we extracted both low-frequency ERPs (1–30 Hz; Figures 4B and 4C) and high-frequency GBOs (>50 Hz; Figures 4E and 4F), as well as their respective current source density (CSD; Figure S2). Nociceptive laser stimuli induced clear GBOs, whose amplitudes were maximal at layers II–IV (Figures 4F and S2B). The CSD estimate revealed a source and a sink in layers I to IV (Figure S2D). Laser-evoked GBOs reliably tracked pain intensity in virtually all cortical layers (Figure 4G). This effect was equally observed when right S1 GBOs were induced by stimuli delivered to the ipsilateral and contralateral sides. By contrast, laser-evoked ERPs encoded both pain intensity and stimulation side (Figure 4D). A complete description of these responses and their modulation is provided in the supplemental information (Figure S2; Data S1).

To identify single-unit spiking related to the experimental conditions, we performed a two-way repeated-measures analysis of variance (ANOVA) with two factors ("intensity": low and high; "side": left and right) (Figures S3A and S3B). This analysis allowed us to categorize single units into five groups: neurons modulated by (1) intensity only, (2) side only, (3) both intensity and side, (4) intensity × side interaction, and (5) none of the previous (Figures S3C–S3E). Only 6 neurons showed a significant intensity × side interaction. Therefore, groups 4 and 5 were not included in further analyses. Neurons in groups 1, 2, and 3 were first divided into putative Pyr neurons and interneurons based on their spike durations (Figure S1F) and then sorted according to their layer location (Figure 4H). Group 1 (modulated by intensity only) contained 59% of recorded units and was composed of 40 interneurons and 31 Pyr neurons (Figure 4I). Group 2 (modulated by side only) contained 18% of units and was composed of 15 Pyr neurons and 7 interneurons (Figure 4I).

To assess the contribution of these units to GBOs, we calculated the spike-triggered field potentials and their phase synchronization (Figures 4J–4L). GBO amplitude was predominantly determined by interneurons of group 1 encoding intensity rather than those of groups 2 and 3 ($p_{[\text{intensity vs. side}]} = 0.02$, $p_{[\text{intensity vs. both}]} = 0.0002$; Figure 4L). In addition, GBOs were phase-locked to the spike activity of group 1 neurons (p values = 0.011), but not that of groups 2 and 3 (p values ≥ 0.1; Figure 4K). The relationship between single-unit activity and ERPs is reported in Figures S3F–S3H.

In experiment 3, we tested whether GBOs were also induced by non-nociceptive somatosensory stimuli, which we delivered at two intensities (low and high) to the left and right forepaws of 14 adult male rats (Figure 1B; see STAR Methods for experimental design). These stimuli elicited negligible withdrawal behavior (compare Figures 4A and 5A), which was, however, clearly modulated by stimulus intensity ($F(1,13) = 32.43$, $p < 0.0001$; Figure 5A). Non-nociceptive stimuli did not elicit clear GBOs in the same time window of GBOs observed in experiment 2 (compare Figures 4E and 5E). 2 × 2 ANOVA confirmed that the amplitude in this gamma window was not modulated by perceptual intensity and stimulation side (Figure 5G). Notably, non-nociceptive stimuli elicited a much earlier phase-locked, time-domain ERP deflection, peaking at 10–50 ms post-stimulus, whose frequency was >30 Hz (Figures 5E and 5F). This peak and its time-frequency representation were not modulated by perceptual intensity but by stimulation side (Figure 5G).

In experiment 3, we also classified neurons into 5 groups, as described for experiment 2, and examined their activity in relation to the time-frequency activity corresponding to the early deflection in the time domain (high-frequency responses [HFRs]: 10–50 ms, 30–100 Hz). This HFR activity was phase-locked to the spiking of neurons in groups 1–3 (p values ≤ 0.03; Figure 5K), and its amplitude was largest when triggered by the spiking of Pyr neurons of group 2 (encoding side only, $p_{[\text{intensity vs. side}]} = 0.019$; Figure 5L). A complete description of these results is provided in the supplemental information (Figures S4 and S5; Data S1).

To rule out the possibility that nociceptive-evoked GBOs reflect motion-related activity, we performed experiment 4, which was identical to experiment 2, except that electrophysiological data were collected from the right M1. As in experiment 2, nocifensive behaviors evoked by laser stimuli were significantly modulated by stimulus intensity ($F(1,5) = 66.3$, $p = 0.0005$), but not by stimulation side ($F(1,5) = 0.3449$, $p = 0.5825$), and there was no interaction between these factors ($F(1,5) = 0.1128$, $p = 0.7506$; Figure S6A). Laser-evoked ERPs and GBOs were also measured in M1 (Figures S6B and S6E), although they showed a different layer distribution as compared with the same responses measured in S1 (Figures 4C and 4F). Nociceptive-evoked ERPs encoded stimulation side ($F(1,5) = 8.906$, $p = 0.0306$), but not modulated by pain intensity ($F(1,5) = 3.206$, $p = 0.1334$; Figure S6D). Similarly, nociceptive-evoked GBOs showed a trend of encoding stimulation side ($F(1,5) = 6.591$, $p = 0.0502$) but did not encode pain intensity ($F(1,5) = 0.342$, $p = 0.584$; Figure S6G). No significant interactions were observed for both ERPs ($F(1,5) = 1.487$, $p = 0.2771$) and GBOs ($F(1,5) = 0.131$, $p = 0.7325$).

Given that interneurons are heterogeneous and cannot be conclusively differentiated by *in vivo* electrophysiology,[28] in experiment 5, we used calcium imaging to specifically test whether PV interneurons tracked pain intensity and compared their response properties to those of Pyr neurons.

Pain intensity is encoded by PV S1 interneurons (experiment 5)

In experiment 5, we tested directly the respective contribution of interneurons and Pyr neurons in encoding pain intensity by collecting calcium imaging data from S1 of freely moving mice (Figure 1E). We were interested in PV-expressing interneurons, as they constitute the largest subpopulation of cortical GABAergic interneurons[29,30] and have been indicated to be involved in nociceptive processing.[7,31] To this end, we injected a Cre

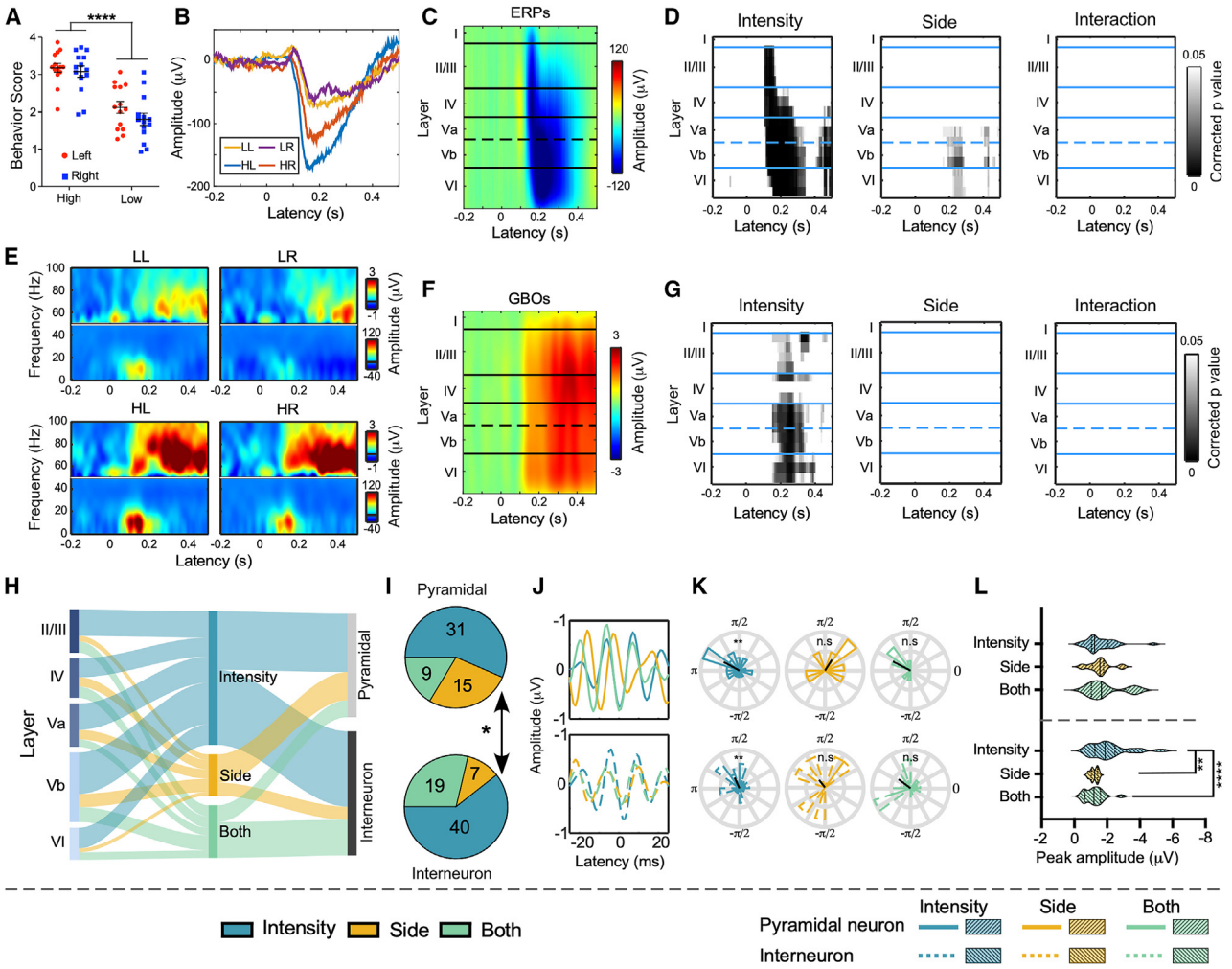

Figure 4. Electrophysiological responses evoked by nociceptive laser stimuli in S1 mainly encoded pain intensity (experiment 2)

(A) Behavioral scores were significantly modulated by stimulus intensity (****$p < 0.0001$, two-way repeated-measures ANOVA). Data were presented as mean ± SEM.

(B) ERP responses (1–30 Hz) averaged across depths for each experimental condition (LL, LR, HL, and HR: low and high intensity for left and right paws, respectively).

(C) Spatiotemporal distributions of ERP responses showed stronger activations in deep layers (Va–VI).

(D) Spatiotemporal distributions of statistical results of ERP responses. The responses at 100–300 ms after stimulus onset were significantly modulated by pain intensity in almost all layers (II/III–VI, left). The responses at 200–300 ms after stimulus onset were significantly modulated by stimulation side in deep layers (Va–VI, middle).

(E) Time-frequency distributions of electrophysiological responses averaged across depths for each experimental condition. High pain trials had stronger power increases than low pain trials at gamma-band frequencies (>50 Hz).

(F) Spatiotemporal distributions of GBOs showed stronger responses in superficial layers (II–IV).

(G) Spatiotemporal distributions of statistical results of GBO responses. The responses at 100–300 ms after stimulus onset were significantly modulated by pain intensity in almost all layers (II/III–VI, left).

(H) Sankey plots of functional differentiation of Pyr neurons and interneurons in different S1 layers. The majority of neurons encoded pain intensity.

(I) Pie charts revealed a significant disparity in the preferred function of Pyr neurons and interneurons (*$p < 0.05$, chi-squared test).

(J–L) Comparisons of spike-triggered GBOs evoked by laser stimuli. GBO amplitudes were significantly larger when triggered by the spikes of interneurons encoding pain intensity (L). Moreover, GBOs were only phase-locked to the spikes of neurons encoding pain intensity (K, **$p < 0.01$, ****$p < 0.0001$, unpaired t test or Mann-Whitney test).

See also Figures S1–S3.

recombinase-dependent viral vector driving the expression of GCaMP6 (AAV-EF1α-DIO-GCaMP6f) into the hindlimb area of S1 in PV-Cre mice (Figure 6A), a procedure that specifically labels PV interneurons. To compare the responses of PV interneurons to Pyr neurons, we labeled Pyr neurons by injecting a CaMKIIα recombinase-dependent viral vector driving GCaMP6 (AAV-CaMKIIα-GCaMP6f) into the same S1 area of wild-type (WT) mice (Figure 6A). We delivered nociceptive laser stimuli of two intensities (low and high) to the left and right hindpaws (Figure 6A) and simultaneously measured neuronal activity from 144

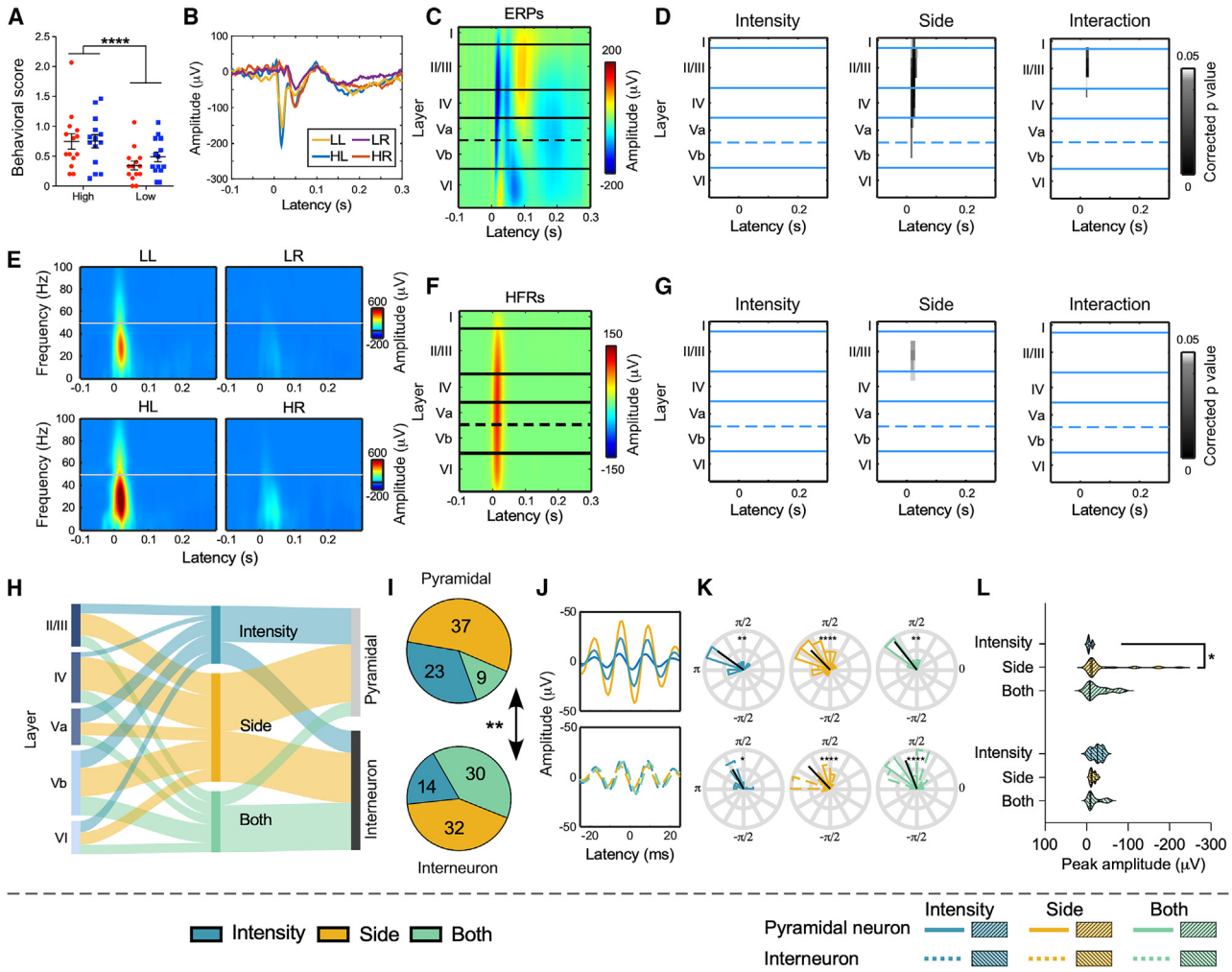

Figure 5. Electrophysiological responses evoked by non-nociceptive electrical stimuli in S1 mainly encoded stimulation side (experiment 3)

(A) Behavioral scores were significantly modulated by stimulus intensity (****$p < 0.0001$, two-way repeated-measures ANOVA). Data were presented as mean ± SEM.

(B) ERP responses (1–30 Hz) averaged across depths for each experimental condition (LL, LR, HL, and HR: low and high intensity for left and right paws, respectively).

(C) Spatiotemporal distributions of ERP responses.

(D) Spatiotemporal distributions of statistical results of ERP responses. The responses at 20–40 ms after stimulus onset were significantly modulated by stimulation side in almost all layers (I–Vb, middle) and also significantly modulated by the intensity × side interaction in superficial layers (II–III, right).

(E) Time-frequency distributions of electrophysiological responses averaged across depths for each experimental condition. Electrical stimuli delivered to the left paw evoked stronger power increases than those delivered to the right paw at all frequencies. This response was the phase-locked, time-frequency counterpart of the early ERP response, and its amplitude dwarfed all later-occurring time-frequency responses.

(F) Spatiotemporal distributions of high-frequency responses (HFRs) extracted from the time-frequency distributions.

(G) Spatiotemporal distributions of statistical results of HFR responses. The responses at 18–35 ms after stimulus onset, corresponding to the time domain deflection around the same latency, were only significantly modulated by stimulation side in superficial layers (middle).

(H) Sankey plots of functional differentiation of Pyr neurons and interneurons in different S1 layers. The majority of neurons encoded stimulation side.

(I) Pie charts revealed a significant disparity in the preferred function of Pyr neurons and interneurons (**$p < 0.01$, chi-squared test).

(J–L) Comparisons of spike-triggered HRF responses evoked by electrical stimuli. HRF amplitudes were significantly larger when triggered by spikes of Pyr neurons encoding stimulation side (L). These responses were phase-locked to the spike activity of all types of neurons (K, *$p < 0.05$, **$p < 0.01$, ****$p < 0.0001$, unpaired t test or Mann-Whitney test).

See also Figures S4–S6.

Pyr neurons in five WT mice (Figure 6G) and from 122 PV interneurons in three PV-Cre mice (Figure 6C). Two-way repeated-measures ANOVA showed that the average firing rates of PV interneurons were modulated by pain intensity ($F(1,121) = 42.21$, $p < 0.0001$; Figure 6D), while those of Pyr neurons were modulated by stimulation side ($F(1,143) = 14.59$, $p < 0.001$; Figure 6F).

We classified PV interneurons and Pyr neurons into the same three functional groups as in experiment 2. Consistent with the

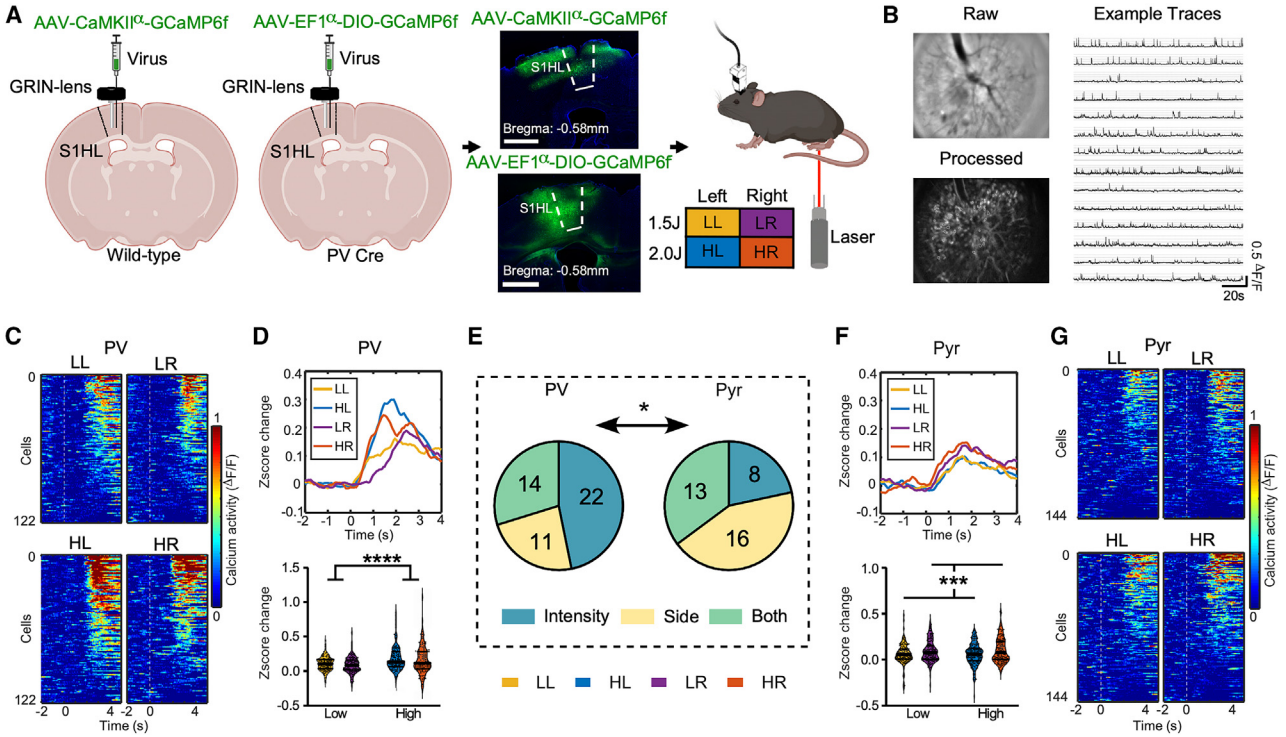

Figure 6. Calcium signal changes of PV interneurons and Pyr neurons in S1 to nociceptive laser stimuli (experiment 5)

(A) Schematic of surgeries (left diagrams), GCaMP expression in left hindpaw of S1 (S1HL; middle images: top, Pyridal neurons; bottom, PV interneurons; scale bars, 500 μm), and calcium imaging experimental design in freely moving mice (right diagram). Nociceptive laser stimuli with two intensities (1.5J and 2J) were delivered to the right and left hindpaws in a pseudorandom order (LL, LR, HL, and HR: low and high intensity for left and right paws, respectively).

(B) Left: raw (top) and processed (bottom) field of view within a region of interest (ROI) derived from a representative calcium imaging session. Right: Example traces of the extracted calcium fluorescence signals obtained from the representative ROI within the imaging session.

(C) Laser-evoked calcium signals averaged across trials (normalized to [0,1]) for PV interneurons in response to low- and high-intensity laser stimuli, administered to the left and right hindpaws, respectively.

(D) Top: time courses of calcium signal changes of PV interneurons in different experimental conditions, spanning from −2 to 4 s. Bottom: firing rates of PV interneurons showed significant differences between high and low intensities, irrespective of stimulation side (****$p < 0.0001$, two-way repeated-measures ANOVA).

(E) Pie charts revealed a significant disparity in the preferred function of PV interneurons (left) and Pyr neurons (right). PV interneurons contained more intensity-encoded neurons and fewer side-encoded neurons than Pyr neurons (*$p < 0.05$, chi-squared test).

(F) Top: time courses of calcium signal changes of Pyr neurons in different experimental conditions, spanning from −2 to 4 s. Bottom: firing rates of Pyr neurons showed significant differences between left and right stimulation sides, irrespective of pain intensity (***$p < 0.001$, two-way repeated-measures ANOVA).

(G) Laser-evoked calcium signals averaged across trials (normalized to [0,1]) for Pyr neurons in response to low- and high-intensity laser stimuli, administered to the left and right hindpaws, respectively.

This figure was created with BioRender.com.

electrophysiological findings, the proportion of Pyr neurons vs. interneurons varied across functional groups: more Pyr neurons encoded side, whereas more interneurons encoded intensity ($x^2 = 6.396$, $p = 0.041$; Figure 6E).

Interneurons, but not Pyr neurons, in S1 causally regulate nocifensive behaviors (experiment 6)

To explore the causal role of the activity of different classes of S1 neurons on nocifensive behaviors, we used optogenetics in freely moving mice to selectively manipulate the activity of PV interneurons and Pyr neurons (Figure 1F). To manipulate PV interneurons, we injected a Cre recombinase-dependent viral vector expressing channelrhodopsin (ChR2) or halorhodopsin (NpHR) into the left S1 of PV-Cre mice and implanted optical fibers above this brain area (Figures 7A and 7B). To manipulate Pyr neurons, we injected a CaMKIIα recombinase-dependent viral vector expressing ChR2 or NpHR into S1 of WT mice and implanted optical fibers above the same brain region (Figures 7A and 7B). For each laser trial, optogenetic stimulation was delivered for 10 s, starting ∼5 s before laser stimulus onset.

Optogenetic activation of PV interneurons did not elicit any overt behavior per se but increased nocifensive behaviors in response to both contralateral and ipsilateral hindpaw stimulation ($F(1,9) = 31.39$, $p = 0.0003$), while their optogenetic inhibition attenuated nocifensive behaviors ($F(1,8) = 12.40$, $p = 0.0078$), especially in response to stimulation of the contralateral hindpaw ($p = 0.0042$; Figure 7C, top). Conversely, there was no significant modulation when the activity of Pyr neurons was enhanced or inhibited (p values ≥ 0.35; Figure 7C, bottom).

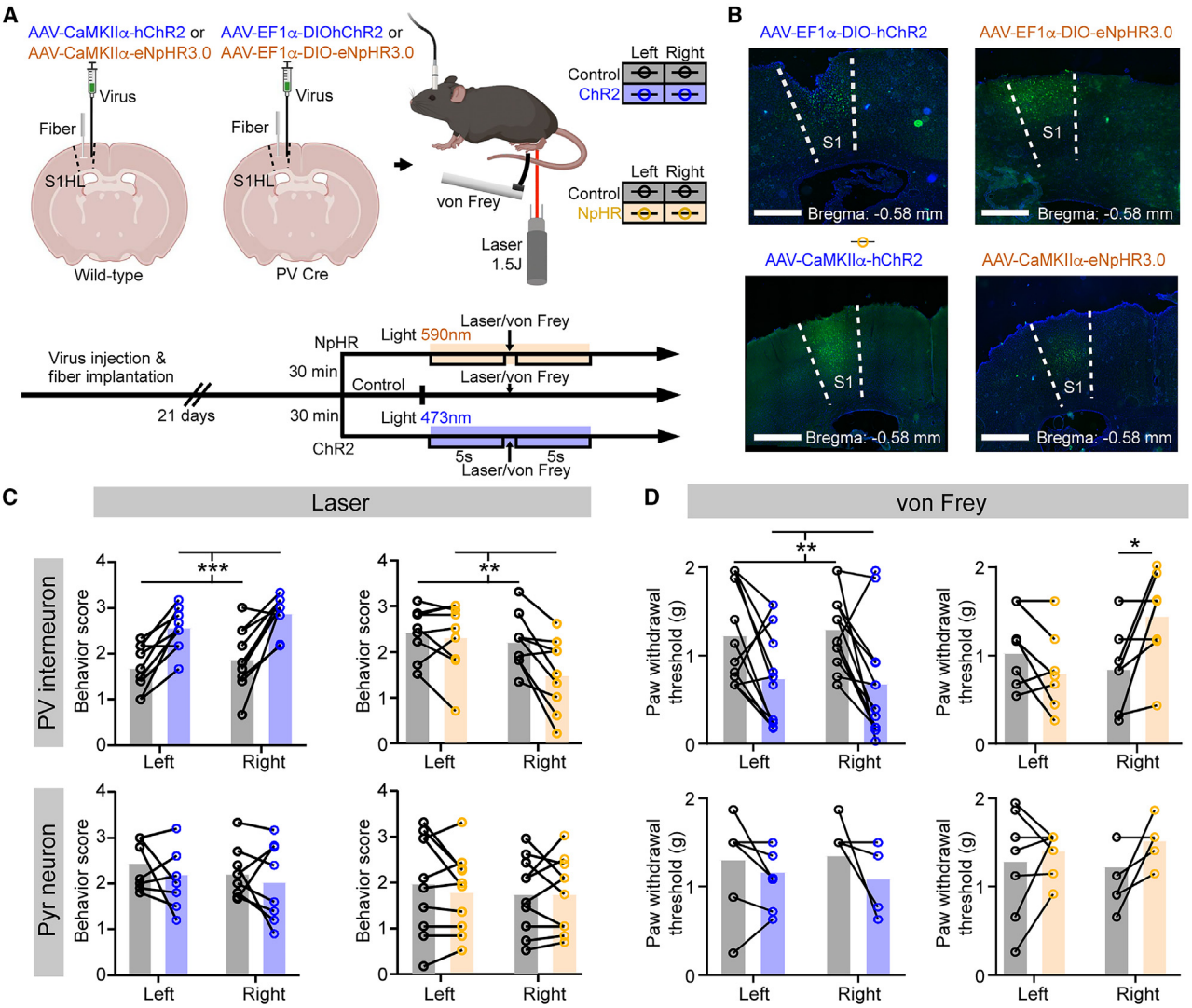

Figure 7. The influence of optogenetic regulation of Pyr neurons and PV interneurons in S1 on pain-related behaviors (experiment 6)

(A) Schematic of surgeries and experimental design for the optogenetic regulation of Pyr neurons and PV interneurons in S1. Nociceptive stimuli, including laser and mechanical stimuli, were delivered to the right and left hindpaws of freely moving mice. The activation of ChR2 using blue light (473 nm) activated the neurons in S1, while the activation of eNpHR3.0 with yellow light (593 nm) inhibited their activity.

(B) Representative images of ChR2 (left) or NpHR (right) expression in S1. Top: PV interneurons; bottom: Pyr neurons. Scale bars: 500 μm.

(C and D) The modulation of pain-related behaviors evoked by laser (C, behavioral score) and mechanical (D, paw withdrawal threshold) stimuli through optogenetic activation or inhibition of Pyr neurons and PV interneurons in S1. PV interneurons in S1, but not Pyr neurons, demonstrated significant regulatory effects, both enhancing and inhibiting pain-related behaviors to right and left hindpaw stimuli (*$p < 0.05$, **$p < 0.01$, ***$p < 0.001$; two-way repeated-measures ANOVA with Bonferroni correction).

This figure was created with BioRender.com.

To test the generalizability of these causal effects beyond thermal pain, we also used a standard mechanical pain assay: the withdrawal threshold to von Frey stimuli delivered to the right and the left hindpaws. Similar to the thermal pain results, activating PV interneurons of the left S1 decreased paw withdrawal thresholds on both sides ($F(1,9) = 11.34$, $p = 0.0063$), indicating increased sensitivity to mechanical pain. Conversely, inhibiting PV interneurons resulted in an increased withdrawal threshold to contralateral stimulation ($p = 0.0057$; Figure 7D, top). Again, there were no clear modulation effects when activating or inhibiting S1 Pyr neurons (p values ≥ 0.14; Figure 7D, bottom).

The activity of PV interneurons in S1 causally regulates nociceptive-evoked GBOs (experiment 7)

In experiment 7, we assessed the causal influence of the activity of different classes of S1 neurons on the electrophysiological responses to nociceptive stimulation. To this end, we used optetrodes, which allow the combining of optogenetics with electrophysiological recordings (Figure 1F). We performed the same

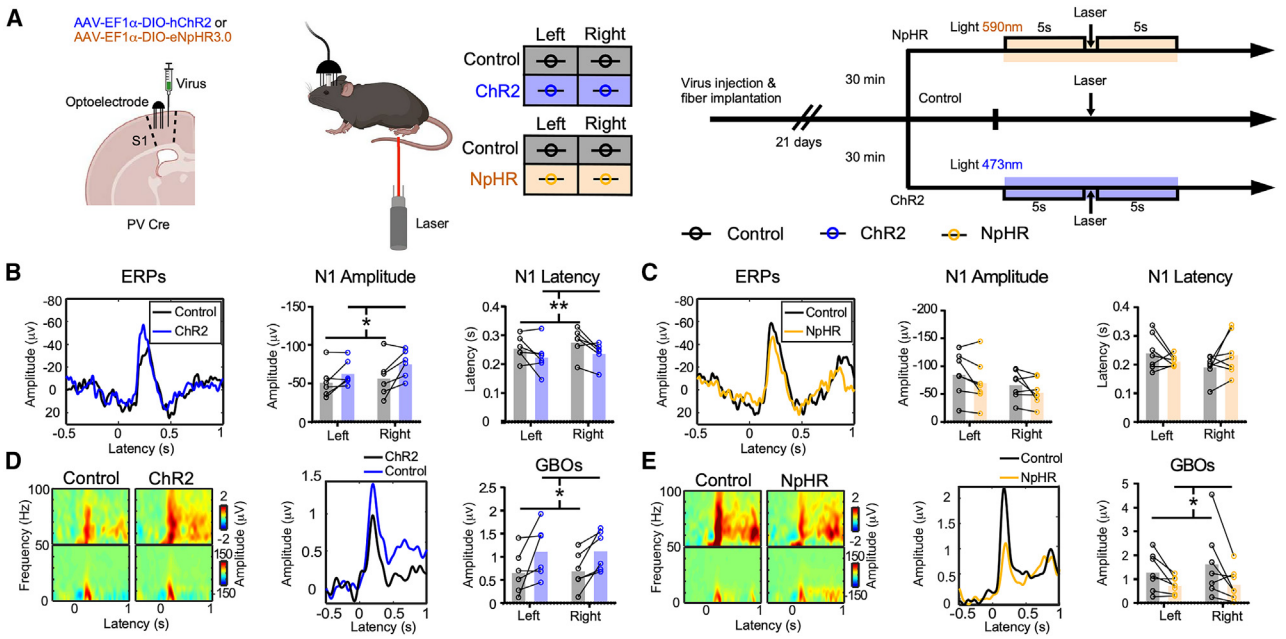

Figure 8. Effect of optogenetic regulation of PV interneurons in S1 on laser-evoked electrophysiological responses (experiment 7)

(A) Schematic of surgery and experimental design for opto-electrophysiological manipulating/recording of PV interneurons in S1 of PV-Cre mice. Nociceptive laser stimuli of a fixed intensity were delivered to the right and left hindpaws of freely moving mice.

(B and C) Average ERP responses (1–30 Hz) for different optogenetic light stimulation conditions: ChR2 (B) and NpHR (C). The activation of PV interneurons led to a significant increase in N1 amplitude and a significant decrease in N1 latency. By contrast, the inhibition of PV interneurons did not result in a significant modulation of N1 amplitude or latency (*$p < 0.05$, **$p < 0.01$; two-way repeated-measures ANOVA).

(D and E) Average time-frequency distributions of electrophysiological responses (left) and GBO time courses (middle) for different optogenetic light stimulation conditions: ChR2 (D) and NpHR (E). The activation of PV interneurons led to a significant increase in GBO amplitude (D), and the inhibition of PV interneurons resulted in a significant decrease in GBO amplitude (E) (*$p < 0.05$, two-way repeated-measures ANOVA).

This figure was created with BioRender.com.

See also Figures S7 and S8, Table S1, and Data S1.

viral injection protocol as in experiment 6 and implanted the optetrodes at the same viral injection site (Figure 8A).

We first replicated, in a different group of animals, the findings of experiment 6: activating PV interneurons increased nocifensive behaviors while inhibiting them decreased these behaviors (Figure S7A). In line with these behavioral findings, the activation of S1 interneurons enhanced nociceptive-evoked GBOs (100–300 ms, 50–100 Hz; $F(1,5) = 8.483$, $p = 0.033$), whereas the inhibition of S1 interneurons decreased them ($F(1,6) = 6.123$, $p = 0.048$; Figures 8D and 8E).

By contrast, optogenetic stimulation of S1 Pyr neurons did not modulate nocifensive behaviors and nociceptive-evoked GBOs (Figures S7B, S7F, and S7G). These results support the idea that S1 Pyr neurons are weakly related, if related at all, to nociceptive-evoked GBOs. The effect of optogenetic stimulation on the laser-evoked responses is reported in the supplemental information (Figure S7; Data S1).

DISCUSSION

In this work, we conclusively demonstrated the neuronal underpinnings of GBOs induced by nociceptive stimuli causing pain. We obtained three main sets of findings. (1) In experiments 1–4, we confirmed the phenomenology and functional properties of GBOs measured at scalp level (in humans) and invasively from S1 and M1 (in rodents), showing that S1 GBOs preferentially encode pain intensity across species. (2) In experiments 2 and 5, we demonstrated that GBOs elicited by nociceptive stimuli are tightly coupled and primarily triggered by spikes of a population of PV-positive S1 interneurons preferentially responsive to pain intensity. (3) In experiments 6 and 7, we optogenetically manipulated the activity of PV-positive S1 interneurons and thereby showed that they causally modulate both GBOs and nocifensive behaviors elicited by nociceptive somatosensory stimuli.

Nociceptive and non-nociceptive LFPs differentially encode the intensity and location of somatosensory perception

Both nociceptive and non-nociceptive stimuli elicited LFP responses in S1 with a similar distribution across cortical layers (Figures S2A and S4A). The corresponding CSDs were consistent with the typical physiological landmarks (Figures S1C–S1E) associated with sensory stimuli in their respective primary cortices, as previously observed for visual,[32] auditory,[33] and barrel cortex stimulation.[34] However, electrophysiological results in S1 (experiments 2 and 3) indicated a clear functional distinction in the landscape of the LFP and single-unit responses to pain and touch. Nociceptive stimuli elicited non-phase-locked

GBOs encoding pain intensity (Figure 4G), as well as phase-locked ERPs encoding both pain intensity and location (Figure 4D). It is important to highlight that the observed correlation between ERP responses and pain intensity is not obligatory, given that it can be easily disrupted by dissociating pain from saliency, for example, when nociceptive stimuli become predictable due to their repetition.[35] This is not the case for GBOs, which more obligatorily reflect perceived pain intensity in both human volunteers and animal models.[5] Importantly, the correlation between GBOs and pain remained significant even after normalizing pain ratings and GBO amplitudes within each stimulus intensity. This suggests that at least part of the relationship between nociceptive-evoked GBOs and pain is not consequent to stimulus intensity (Figure 3A).

By contrast, non-nociceptive stimuli evoked phase-locked neural responses in S1 with a much earlier latency and a much larger amplitude (~20 ms and >200 μV; Figure 5B) than those of responses evoked by nociceptive stimuli (~150 ms and <150 μV; Figure 4B). These early-latency non-nociceptive responses displayed a clear ability to encode stimulus location, like the N20 component of the early-latency scalp or epidural potentials evoked by median nerve stimulation in humans.[36] The high-frequency part of these responses was only present when stimuli were delivered to the contralateral side and, within the range of stimulus intensity used in the current experiments, did not encode reflective behaviors (Figure 5G). The findings that phase-locked neural responses elicited by non-nociceptive stimuli mainly encode tactile locations align with the principles of lateralized representation of touch and the role of S1 in tactile processing.[37,38]

Electrophysiological data collected from M1 (experiment 4) showed that both phase-locked ERPs and non-phase-locked GBOs in M1 evoked by nociceptive stimuli encode stimulus location, but not pain intensity (Figure S6G). This observation is crucial as it suggests the selectivity of S1 compared with M1 in being the source of GBOs that encode pain intensity and rules out the possibility that GBOs measured in S1 reflect motor-related responses. This finding is also consistent with a previous study excluding M1 as the source of nociceptive-evoked GBOs.[18] Indeed, nociceptive-evoked GBOs have a shorter latency than pain-related behaviors.[5] GBOs peak first at S1 and then at M1, and optogenetically inducing GBOs in M1 does not cause hypersensitivity to nociceptive stimuli.[7]

PV interneurons, rather than Pyr neurons, encode nocifensive behavior

A distinct encoding strategy was observed for different neuron types: when using spike duration to classify units according to their putative type, the majority of nociresponsive interneurons encoded pain intensity (61%; Figure 4I), whereas a large proportion of Pyr neurons responding to non-nociceptive stimuli encoded stimulation side (54%; Figure 5I). This different contribution of neuron types in encoding stimulus properties was also found in auditory[39] and gustatory[40] cortices. It is important to note that the electrophysiological approach used here and in our previous study did not allow us to distinguish Pyr neurons from interneurons with certainty and is entirely blind to neuronal subtypes.[28] To solve these issues, we recorded calcium signals of individual PV interneurons and Pyr neurons within S1. The results provided direct and strong evidence that PV interneurons primarily associated with variations in nocifensive behavior, while Pyr neurons mainly encoded stimulus location (Figure 6). Such distinct encoding strategies support the notion that different types of neurons play distinct roles in nociceptive processing.[41,42] Notably, PV interneurons and non-phase-locked GBOs evoked by nociceptive stimuli shared similar encoding strategies for pain perception, suggesting that PV interneurons may serve as the neural substrate for the encoding of pain intensity by GBOs (Figure 4).

PV S1 interneurons drive nociceptive-evoked GBOs in S1

Spike-triggered LFP analyses allowed us to relate spiking activity to GBOs. GBOs elicited by nociceptive stimuli were predominantly driven by S1 interneurons encoding pain intensity (Figure 4K). These findings replicate, in a different group of subjects, our previous observation that GBOs recorded from the scalp in response to nociceptive stimuli originate from S1 interneurons.[18] However, the electrophysiological approach was only correlational. To provide causal evidence supporting the aforementioned inference, we directly manipulated the activities of PV interneurons and Pyr neurons through optogenetics.[43] Modulating PV interneurons exerted a consistent and profound influence on nociceptive-evoked GBOs: activating PV interneurons increased GBOs, while inhibiting them decreased GBOs (Figures 8D and 8E). By contrast, neither the activation nor the inhibition of Pyr neurons had significant effects on nociceptive-evoked GBOs (Figures S7F and S7G). These findings provide solid causal evidence pinpointing PV S1 interneurons as the neuronal source of nociceptive-evoked GBOs.

Previous studies have shown that PV interneurons can modulate spontaneous GBOs and that enhancing spontaneous GBOs using optogenetics increase pain behaviors.[7,19] However, these studies have not elucidated how PV interneurons contribute to GBOs evoked by nociceptive stimuli, i.e., the neural responses elicited by real-life nociceptive stimuli causing pain. Please note that in our study, 40 Hz optogenetic stimulation only modulated spontaneous GBOs at ~40 Hz, i.e., the same frequency of the delivered light stimulation. By contrast, optogenetic stimulation did not modulate spontaneous GBOs at higher frequencies (i.e., 60–90 Hz), the frequencies typically evoked by nociceptive stimuli (Figure S8). These results suggest that spontaneous GBOs and nociceptive-evoked GBOs may be generated with distinct mechanisms. Our current findings provide the first demonstration that nociceptive-evoked GBOs generated by PV interneurons within S1 exert a causal influence on pain experience.

In agreement with the activity of nociresponsive PV interneurons in bilateral S1, nociceptive-evoked GBOs recorded from the human scalp showed a topography with symmetrical activity, maximal at central electrodes.[25] Indeed, GABAergic interneurons, and particularly the fast-spiking PV interneurons that fire rhythmically at gamma frequencies,[44] play a pivotal role in shaping synchronous activity patterns within the brain.[19,45,46] This is consequent to the high degree of direct coupling of PV interneurons through gap junctions, which fosters the synchronization of their firing patterns.[47] Therefore, the synchronization

of the firing of PV interneurons in bilateral S1 is responsible for the generation of coherent GBOs that can also be measured non-invasively in humans using scalp EEG.

A thalamocortical mechanism explaining the different strategies of PV interneurons and Pyr neurons in encoding nociceptive input

We showed that, within S1, PV interneurons and Pyr neurons mainly encode nocifensive behavior and stimulus location, respectively. However, one question remains: why do these neurons have different encoding strategies, even though both receive thalamic inputs and tightly interact with each other?

PV interneurons' encoding strategy may be explained by the bilateral activation of these interneurons consequent to their cortico-cortical projections.[48] Indeed, coupling between oscillators in the two hemispheres is established by long-range interneurons.[49] Notably, the distally projecting axons of long-range interneurons have larger-diameter myelin sheaths than those of Pyr neurons, which allows for fast axon conduction velocity, a prerequisite for establishing gamma synchrony.[50] Long-range projections from S1 contralateral to the side of nociceptive stimulation could strongly recruit ipsilateral PV interneurons and lead to PV interneuron-mediated feedforward inhibition of Pyr neurons in the ipsilateral S1.[47] The interhemispheric projections of PV interneurons may explain why modulating these neurons in unilateral S1 could induce bilateral changes in neural responses evoked by nociceptive stimuli (Figure 8). Although our study could not test whether inter-hemispheric communication is essential for GBO generation, future studies may directly modulate this communication to test our explanation of PV interneurons' encoding strategy.

Theoretically, both Pyr neurons and PV interneurons could encode the intensity of nociceptive stimulation, as stronger nociceptive input drives more strongly than thalamocortical third-order neurons. However, only PV interneurons exhibited higher firing rates in trials with strong nocifensive behaviors than those with weak behaviors (Figure 6). A possible explanation is that when receiving high-intensity nociceptive stimuli, PV interneurons locally inhibit Pyr neurons, thus disrupting the association between the firing rates of Pyr neurons and pain intensity. This explanation is supported by the finding that PV interneurons fire at more consistent times relative to the thalamocortical afferent stimulation and inhibit the afferent-locked spike timing in Pyr neurons.[51,52] Although our study does not provide direct evidence that optogenetic manipulation of PV interneurons affects Pyr neurons in S1, it provides indirect evidence that such manipulation can modulate low-frequency ERP responses (1–30 Hz), which are thought to originate from the collective activity of Pyr neurons[53] (Figures 8B and 8C). The complex interaction between PV interneurons and Pyr neurons in S1 should be investigated more thoroughly in the future.

Conclusion and caveats

This study represents a significant step forward by sampling nociceptive-evoked neural activity across different scales. Specifically, it bridges from the microscopic level of the activity of individual PV interneurons to the mesoscopic level of GBOs and thereby establishes a solid foundation for developing pain assessment and treatment in practice, such as neuromodulation for clinical pain.[54] Nevertheless, the study has a number of limitations. First, we only focused on the activity of PV interneurons and Pyr neurons. Future work should investigate the responsiveness to nociceptive stimuli of other GABAergic interneurons, such as those expressing the vasoactive intestinal peptide or somatostatin, as they may also play significant roles in nociceptive processing within S1.[47] Second, although we explored the laminar profiles of LFP responses and spike activities, subsequent calcium imaging and optogenetic modulation were limited to layers IV–Va, given that they contain the highest concentration of neurons.[55,56] Optical imaging and optogenetics across different cortical layers will provide a more comprehensive understanding of nociceptive processing. Third, we focused on the neural and behavioral responses to transient nociceptive stimuli, and it remains unclear whether our findings can be generalized to sustained pain or chronic pain. Fourth, previous studies showed that GBOs have been associated with other aspects of pain, such as pain affect,[13] motor responses to pain,[14,15] and predictive error coding of pain.[9,16] Although this study confirmed the role of S1 GBOs in encoding pain intensity, we cannot rule out their involvement in other functions, especially for GBOs generated from other brain regions, and it is of interest to investigate the neuronal mechanisms of GBOs related to these functions in future studies.

RESOURCE AVAILABILITY

Lead contact

Requests for further information and for resources and reagents should be directed to and will be fulfilled by the lead contact, Li Hu (huli@psych.ac.cn).

Materials availability

This study did not generate new, unique reagents.

Data and code availability

The raw electrophysiological and calcium imaging data generated in this study have been deposited in the ScienceDB database and are publicly available as of the date of publication at https://doi.org/10.57760/sciencedb.11364. All original code for analysis and for generating figures has been deposited on GitHub and is publicly available at https://doi.org/10.5281/zenodo.14608070 as of the date of publication. Any additional information required to reanalyze the data reported in this paper is available from the lead contact upon request.

ACKNOWLEDGMENTS

This work is supported by "Sci-Tech Innovation 2030" Brain Science and Brain-Inspired Intelligence Technology Research by the Ministry of Science and Technology of China (2022ZD0206400); National Natural Science Foundation of China (32000749 and 32071061); Beijing Natural Science Foundation (JQ22018); Key Lab for Neuroscience, Ministry of Education of China, Peking University; and National Health Commission of China, Peking University. We thank Dr. Longyu Ma from Peking University for help on electrophysiological experiments.

AUTHOR CONTRIBUTIONS

Conceptualization, L.Y., G.D.I., and L.H.; methodology, L.Y. and C.B.; investigation, L.Y., C.B., and W.Z.; formal analysis, L.Y. and C.B.; data curation, L.Y.; writing – original draft, L.Y. and C.B.; writing – review & editing, L.Y., C.B., L.Z., F.Z., G.D.I., and L.H.; supervision, G.D.I. and L.H.; funding acquisition, L.Y. and L.H.

DECLARATION OF INTERESTS

The authors declare no competing interests.

STAR★METHODS

Detailed methods are provided in the online version of this paper and include the following:

- KEY RESOURCES TABLE
- EXPERIMENTAL MODEL AND STUDY PARTICIPANT DETAILS
- METHOD DETAILS
  - Surgical procedures
  - Experimental design and sensory stimuli
  - Data collection
- QUANTIFICATION AND STATISTICAL ANALYSIS
  - Data preprocessing
  - Time-domain and time-frequency domain analyses
  - Linear mixed model (LMM) analysis
  - Current source density (CSD) estimation
  - Spike detection and classification
  - Identification of functionally differentiated neurons
  - Spike-triggered field potentials for functionally differentiated neurons
  - Statistical analysis

SUPPLEMENTAL INFORMATION

Supplemental information can be found online at https://doi.org/10.1016/j.neuron.2024.12.011.

Received: February 6, 2024
Revised: August 2, 2024
Accepted: December 12, 2024
Published: January 13, 2025

REFERENCES

1. Jepma, M., Koban, L., van Doorn, J., Jones, M., and Wager, T.D. (2018). Behavioural and neural evidence for self-reinforcing expectancy effects on pain. Nat. Hum. Behav. *2*, 838–855. https://doi.org/10.1038/s41562-018-0455-8.
2. Melzack, R., and Wall, P.D. (1988). The Challenge of Pain, Revised Edition (Penguin Books).
3. Davis, K.D., Flor, H., Greely, H.T., Iannetti, G.D., Mackey, S., Ploner, M., Pustilnik, A., Tracey, I., Treede, R.D., and Wager, T.D. (2017). Brain imaging tests for chronic pain: medical, legal and ethical issues and recommendations. Nat. Rev. Neurol. *13*, 624–638. https://doi.org/10.1038/nrneurol.2017.122.
4. Mouraux, A., and Iannetti, G.D. (2018). The search for pain biomarkers in the human brain. Brain *141*, 3290–3307. https://doi.org/10.1093/brain/awy281.
5. Hu, L., and Iannetti, G.D. (2019). Neural indicators of perceptual variability of pain across species. Proc. Natl. Acad. Sci. USA *116*, 1782–1791. https://doi.org/10.1073/pnas.1812499116.
6. Gross, J., Schnitzler, A., Timmermann, L., and Ploner, M. (2007). Gamma oscillations in human primary somatosensory cortex reflect pain perception. PLOS Biol. *5*, e133. https://doi.org/10.1371/journal.pbio.0050133.
7. Tan, L.L., Oswald, M.J., Heinl, C., Retana Romero, O.A., Kaushalya, S.K., Monyer, H., and Kuner, R. (2019). Gamma oscillations in somatosensory cortex recruit prefrontal and descending serotonergic pathways in aversion and nociception. Nat. Commun. *10*, 983. https://doi.org/10.1038/s41467-019-08873-z.
8. Zhang, Q., Hu, S., Talay, R., Xiao, Z., Rosenberg, D., Liu, Y., Sun, G., Li, A., Caravan, B., Singh, A., et al. (2023). A prototype closed-loop brain-machine interface for the study and treatment of pain. Nat. Biomed. Eng. *7*, 533–545. https://doi.org/10.1038/s41551-021-00736-7.
9. Bott, F.S., Nickel, M.M., Hohn, V.D., May, E.S., Gil Ávila, C., Tiemann, L., Gross, J., and Ploner, M. (2023). Local brain oscillations and interregional connectivity differentially serve sensory and expectation effects on pain. Sci. Adv. *9*, eadd7572. https://doi.org/10.1126/sciadv.add7572.
10. Nickel, M.M., Tiemann, L., Hohn, V.D., May, E.S., Gil Ávila, C., Eippert, F., and Ploner, M. (2022). Temporal-spectral signaling of sensory information and expectations in the cerebral processing of pain. Proc. Natl. Acad. Sci. USA *119*, e2116616119. https://doi.org/10.1073/pnas.2116616119.
11. Tiemann, L., May, E.S., Postorino, M., Schulz, E., Nickel, M.M., Bingel, U., and Ploner, M. (2015). Differential neurophysiological correlates of bottom-up and top-down modulations of pain. Pain *156*, 289–296. https://doi.org/10.1097/01.j.pain.0000460309.94442.44.
12. Zhang, Z.G., Hu, L., Hung, Y.S., Mouraux, A., and Iannetti, G.D. (2012). Gamma-band oscillations in the primary somatosensory cortex–a direct and obligatory correlate of subjective pain intensity. J. Neurosci. *32*, 7429–7438. https://doi.org/10.1523/JNEUROSCI.5877-11.2012.
13. Lyu, Y., Zidda, F., Radev, S.T., Liu, H., Guo, X., Tong, S., Flor, H., and Andoh, J. (2021). Gamma band oscillations reflect sensory and affective dimensions of pain. Front. Neurol. *12*, 695187. https://doi.org/10.3389/fneur.2021.695187.
14. Schulz, E., Tiemann, L., Witkovsky, V., Schmidt, P., and Ploner, M. (2012). γ Oscillations are involved in the sensorimotor transformation of pain. J. Neurophysiol. *108*, 1025–1031. https://doi.org/10.1152/jn.00186.2012.
15. Tiemann, L., Hohn, V.D., Ta Dinh, S., May, E.S., Nickel, M.M., Gross, J., and Ploner, M. (2018). Distinct patterns of brain activity mediate perceptual and motor and autonomic responses to noxious stimuli. Nat. Commun. *9*, 4487. https://doi.org/10.1038/s41467-018-06875-x.
16. Strube, A., Rose, M., Fazeli, S., and Büchel, C. (2021). The temporal and spectral characteristics of expectations and prediction errors in pain and thermoception. eLife *10*, e62809. https://doi.org/10.7554/eLife.62809.
17. Gousset, S., Torta, D.M., Mouraux, A., Lambert, J., and van den Broeke, E.N. (2023). Pinprick-induced gamma-band oscillations are not a useful electrophysiological marker of pinprick hypersensitivity in humans. Clin. Neurophysiol. *153*, 102–110. https://doi.org/10.1016/j.clinph.2023.06.018.
18. Yue, L., Iannetti, G.D., and Hu, L. (2020). The neural origin of nociceptive-induced gamma-band oscillations. J. Neurosci. *40*, 3478–3490. https://doi.org/10.1523/JNEUROSCI.0255-20.2020.
19. Sohal, V.S., Zhang, F., Yizhar, O., and Deisseroth, K. (2009). Parvalbumin neurons and gamma rhythms enhance cortical circuit performance. Nature *459*, 698–702. https://doi.org/10.1038/nature07991.
20. Tu, Y., Zhang, Z., Tan, A., Peng, W., Hung, Y.S., Moayedi, M., Iannetti, G.D., and Hu, L. (2016). Alpha and gamma oscillation amplitudes synergistically predict the perception of forthcoming nociceptive stimuli. Hum. Brain Mapp. *37*, 501–514. https://doi.org/10.1002/hbm.23048.
21. Baumgärtner, U., Cruccu, G., Iannetti, G.D., and Treede, R.D. (2005). Laser guns and hot plates. Pain *116*, 1–3. https://doi.org/10.1016/j.pain.2005.04.021.
22. Iannetti, G.D., Zambreanu, L., and Tracey, I. (2006). Similar nociceptive afferents mediate psychophysical and electrophysiological responses to heat stimulation of glabrous and hairy skin in humans. J. Physiol. *577*, 235–248. https://doi.org/10.1113/jphysiol.2006.115675.
23. Bassez, I., Ricci, K., Vecchio, E., Delussi, M., Gentile, E., Marinazzo, D., and de Tommaso, M. (2020). The effect of painful laser stimuli on EEG gamma-band activity in migraine patients and healthy controls. Clin. Neurophysiol. *131*, 1755–1766. https://doi.org/10.1016/j.clinph.2020.04.157.
24. Linde, L.D., Ortiz, O., Choles, C.M., and Kramer, J.L.K. (2023). Pain-related gamma band activity is dependent on the features of nociceptive stimuli: a comparison of laser and contact heat. J. Neurophysiol. *129*, 262–270. https://doi.org/10.1152/jn.00357.2022.

25. Li, Z., Zhang, L., Zeng, Y., Zhao, Q., and Hu, L. (2023). Gamma-band oscillations of pain and nociception: A systematic review and meta-analysis of human and rodent studies. Neurosci. Biobehav. Rev. *146*, 105062. https://doi.org/10.1016/j.neubiorev.2023.105062.

26. Valentini, E., Hu, L., Chakrabarti, B., Hu, Y., Aglioti, S.M., and Iannetti, G.D. (2012). The primary somatosensory cortex largely contributes to the early part of the cortical response elicited by nociceptive stimuli. Neuroimage *59*, 1571–1581. https://doi.org/10.1016/j.neuroimage.2011.08.069.

27. Schulz, E., Zherdin, A., Tiemann, L., Plant, C., and Ploner, M. (2012). Decoding an individual's sensitivity to pain from the multivariate analysis of EEG data. Cereb. Cortex *22*, 1118–1123. https://doi.org/10.1093/cercor/bhr186.

28. Lemon, R.N., Baker, S.N., and Kraskov, A. (2021). Classification of cortical neurons by spike shape and the identification of pyramidal neurons. Cereb. Cortex *31*, 5131–5138. https://doi.org/10.1093/cercor/bhab147.

29. Kuramoto, E., Tanaka, Y.R., Hioki, H., Goto, T., and Kaneko, T. (2022). Local connections of pyramidal neurons to parvalbumin-producing interneurons in motor-associated cortical areas of mice. eNeuro *9*, ENEURO.0567-20.2021. https://doi.org/10.1523/ENEURO.0567-20.2021.

30. Tremblay, R., Lee, S., and Rudy, B. (2016). GABAergic interneurons in the neocortex: from cellular properties to circuits. Neuron *91*, 260–292. https://doi.org/10.1016/j.neuron.2016.06.033.

31. Guo, Z., Ni, H., Cui, Z., Zhu, Z., Kang, J., Wang, D., and Ke, Z. (2023). Pain sensitivity related to gamma oscillation of parvalbumin interneuron in primary somatosensory cortex in Dync1i1(-/-) mice. Neurobiol. Dis. *183*, 106170. https://doi.org/10.1016/j.nbd.2023.106170.

32. Senzai, Y., Fernandez-Ruiz, A., and Buzsáki, G. (2019). Layer-specific physiological features and interlaminar interactions in the primary visual cortex of the mouse. Neuron *101*, 500–513.e5. https://doi.org/10.1016/j.neuron.2018.12.009.

33. El-Tabbal, M., Niekisch, H., Henschke, J.U., Budinger, E., Frischknecht, R., Deliano, M., and Happel, M.F.K. (2021). The extracellular matrix regulates cortical layer dynamics and cross-columnar frequency integration in the auditory cortex. Commun. Biol. *4*, 322. https://doi.org/10.1038/s42003-021-01837-4.

34. Reyes-Puerta, V., Sun, J.J., Kim, S., Kilb, W., and Luhmann, H.J. (2015). Laminar and columnar structure of sensory-evoked multineuronal spike sequences in adult rat barrel cortex in vivo. Cereb. Cortex *25*, 2001–2021. https://doi.org/10.1093/cercor/bhu007.

35. Iannetti, G.D., Hughes, N.P., Lee, M.C., and Mouraux, A. (2008). Determinants of laser-evoked EEG responses: pain perception or stimulus saliency? J. Neurophysiol. *100*, 815–828. https://doi.org/10.1152/jn.00097.2008.

36. Allison, T., McCarthy, G., Wood, C.C., and Jones, S.J. (1991). Potentials evoked in human and monkey cerebral cortex by stimulation of the median nerve. A review of scalp and intracranial recordings. Brain *114*, 2465–2503. https://doi.org/10.1093/brain/114.6.2465.

37. Dijkerman, H.C., and de Haan, E.H.F. (2007). Somatosensory processes subserving perception and action. Behav. Brain Sci. *30*, 189–201. https://doi.org/10.1017/S0140525X07001392.

38. Moseley, G.L., and Vlaeyen, J.W.S. (2015). Beyond nociception: the imprecision hypothesis of chronic pain. Pain *156*, 35–38. https://doi.org/10.1016/j.pain.0000000000000014.

39. Liu, X.P., and Wang, X. (2022). Distinct neuronal types contribute to hybrid temporal encoding strategies in primate auditory cortex. PLOS Biol. *20*, e3001642. https://doi.org/10.1371/journal.pbio.3001642.

40. Yokota, T., Eguchi, K., and Hiraba, K. (2011). Functional properties of putative pyramidal neurons and inhibitory interneurons in the rat gustatory cortex. Cereb. Cortex *21*, 597–606. https://doi.org/10.1093/cercor/bhq126.

41. Ghitani, N., Barik, A., Szczot, M., Thompson, J.H., Li, C., Le Pichon, C.E., Krashes, M.J., and Chesler, A.T. (2017). Specialized mechanosensory nociceptors mediating rapid responses to hair pull. Neuron *95*, 944–954.e4. https://doi.org/10.1016/j.neuron.2017.07.024.

42. Li, L., Rutlin, M., Abraira, V.E., Cassidy, C., Kus, L., Gong, S., Jankowski, M.P., Luo, W., Heintz, N., Koerber, H.R., et al. (2011). The functional organization of cutaneous low-threshold mechanosensory neurons. Cell *147*, 1615–1627. https://doi.org/10.1016/j.cell.2011.11.027.

43. Deisseroth, K. (2015). Optogenetics: 10 years of microbial opsins in neuroscience. Nat. Neurosci. *18*, 1213–1225. https://doi.org/10.1038/nn.4091.

44. Caputi, A., Melzer, S., Michael, M., and Monyer, H. (2013). The long and short of GABAergic neurons. Curr. Opin. Neurobiol. *23*, 179–186. https://doi.org/10.1016/j.conb.2013.01.021.

45. Cardin, J.A., Carlén, M., Meletis, K., Knoblich, U., Zhang, F., Deisseroth, K., Tsai, L.H., and Moore, C.I. (2009). Driving fast-spiking cells induces gamma rhythm and controls sensory responses. Nature *459*, 663–667. https://doi.org/10.1038/nature08002.

46. Isaacson, J.S., and Scanziani, M. (2011). How inhibition shapes cortical activity. Neuron *72*, 231–243. https://doi.org/10.1016/j.neuron.2011.09.027.

47. Naskar, S., Qi, J., Pereira, F., Gerfen, C.R., and Lee, S. (2021). Cell-type-specific recruitment of GABAergic interneurons in the primary somatosensory cortex by long-range inputs. Cell Rep. *34*, 108774. https://doi.org/10.1016/j.celrep.2021.108774.

48. Buzsáki, G., and Wang, X.J. (2012). Mechanisms of gamma oscillations. Annu. Rev. Neurosci. *35*, 203–225. https://doi.org/10.1146/annurev-neuro-062111-150444.

49. Buzsáki, G., and Draguhn, A. (2004). Neuronal oscillations in cortical networks. Science *304*, 1926–1929. https://doi.org/10.1126/science.1099745.

50. Jinno, S., and Kosaka, T. (2006). Cellular architecture of the mouse hippocampus: a quantitative aspect of chemically defined GABAergic neurons with stereology. Neurosci. Res. *56*, 229–245. https://doi.org/10.1016/j.neures.2006.07.007.

51. Krause, B.M., Murphy, C.A., Uhlrich, D.J., and Banks, M.I. (2019). PV+ cells enhance temporal population codes but not stimulus-related timing in auditory cortex. Cereb. Cortex *29*, 627–647. https://doi.org/10.1093/cercor/bhx345.

52. Vecchia, D., Beltramo, R., Vallone, F., Chéreau, R., Forli, A., Molano-Mazón, M., Bawa, T., Binini, N., Moretti, C., Holtmaat, A., et al. (2020). Temporal sharpening of sensory responses by layer V in the mouse primary somatosensory cortex. Curr. Biol. *30*, 1589–1599.e10. https://doi.org/10.1016/j.cub.2020.02.004.

53. Luck, S.J. (2005). An Introduction to the Event-Related Potential Technique (MIT Press).

54. Li, Z.J., Zhang, L.B., Chen, Y.X., and Hu, L. (2023). Advancements and challenges in neuromodulation technology: interdisciplinary opportunities and collaborative endeavors. Sci. Bull. (Beijing) *68*, 1978–1982. https://doi.org/10.1016/j.scib.2023.08.019.

55. Petersen, C.C.H. (2019). Sensorimotor processing in the rodent barrel cortex. Nat. Rev. Neurosci. *20*, 533–546. https://doi.org/10.1038/s41583-019-0200-y.

56. Ayaz, A., Stäuble, A., Hamada, M., Wulf, M.-A., Saleem, A.B., and Helmchen, F. (2019). Layer-specific integration of locomotion and sensory information in mouse barrel cortex. Nat. Commun. *10*, 2585. https://doi.org/10.1038/s41467-019-10564-8.

57. Sariev, A., Chung, J., Jung, D., Sharif, F., Lee, J.Y., Kim, S., and Royer, S. (2017). Implantation of chronic silicon probes and recording of hippocampal place cells in an enriched treadmill apparatus. J. Vis. Exp. *128*, 56438. https://doi.org/10.3791/56438.

58. Yue, L., Zhang, F., Lu, X., Wan, Y., and Hu, L. (2019). Simultaneous recordings of cortical local field potentials and electrocorticograms in response

to nociceptive laser stimuli from freely moving rats. J. Vis. Exp. *143*, e58686. https://doi.org/10.3791/58686.

59. Alloway, K.D., Smith, J.B., and Beauchemin, K.J. (2010). Quantitative analysis of the bilateral brainstem projections from the whisker and forepaw regions in rat primary motor cortex. J. Comp. Neurol. *518*, 4546–4566. https://doi.org/10.1002/cne.22477.
60. Moxon, K.A., Hale, L.L., Aguilar, J., and Foffani, G. (2008). Responses of infragranular neurons in the rat primary somatosensory cortex to forepaw and hindpaw tactile stimuli. Neuroscience *156*, 1083–1092. https://doi.org/10.1016/j.neuroscience.2008.08.009.
61. Paxinos, G., and Watson, C. (2007). The Rat Brain in Stereotaxic Coordinates, Sixth Edition (Academic Press/Elsevier).
62. Hu, L., Cai, M.M., Xiao, P., Luo, F., and Iannetti, G.D. (2014). Human brain responses to concomitant stimulation of Adelta and C nociceptors. J. Neurosci. *34*, 11439–11451. https://doi.org/10.1523/JNEUROSCI.1355-14.2014.
63. Leandri, M., Saturno, M., Spadavecchia, L., Iannetti, G.D., Cruccu, G., and Truini, A. (2006). Measurement of skin temperature after infrared laser stimulation. Neurophysiol. Clin. *36*, 207–218. https://doi.org/10.1016/j.neucli.2006.08.004.
64. Sikandar, S., Ronga, I., Iannetti, G.D., and Dickenson, A.H. (2013). Neural coding of nociceptive stimuli-from rat spinal neurones to human perception. Pain *154*, 1263–1273. https://doi.org/10.1016/j.pain.2013.03.041.
65. Hu, L., Xia, X.L., Peng, W.W., Su, W.X., Luo, F., Yuan, H., Chen, A.T., Liang, M., and Iannetti, G. (2015). Was it a pain or a sound? Across-species variability in sensory sensitivity. Pain *156*, 2449–2457. https://doi.org/10.1097/j.pain.0000000000000316.
66. Peng, W., Lou, W., Huang, X., Ye, Q., Tong, R.K.Y., and Cui, F. (2021). Suffer together, bond together: brain-to-brain synchronization and mutual affective empathy when sharing painful experiences. Neuroimage *238*, 118249. https://doi.org/10.1016/j.neuroimage.2021.118249.
67. Liu, Y., Latremoliere, A., Li, X., Zhang, Z., Chen, M., Wang, X., Fang, C., Zhu, J., Alexandre, C., Gao, Z., et al. (2018). Touch and tactile neuropathic pain sensitivity are set by corticospinal projections. Nature *561*, 547–550. https://doi.org/10.1038/s41586-018-0515-2.
68. Fan, R.J., Kung, J.C., Olausson, B.A., and Shyu, B.C. (2009). Nocifensive behaviors components evoked by brief laser pulses are mediated by C fibers. Physiol. Behav. *98*, 108–117. https://doi.org/10.1016/j.physbeh.2009.04.022.
69. Wang, X., Liu, Y., Li, X., Zhang, Z., Yang, H., Zhang, Y., Williams, P.R., Alwahab, N.S.A., Kapur, K., Yu, B., et al. (2017). Deconstruction of corticospinal circuits for goal-directed motor skills. Cell *171*, 440–455.e14. https://doi.org/10.1016/j.cell.2017.08.014.
70. Fenno, L., Yizhar, O., and Deisseroth, K. (2011). The development and application of optogenetics. Annu. Rev. Neurosci. *34*, 389–412. https://doi.org/10.1146/annurev-neuro-061010-113817.
71. Delorme, A., and Makeig, S. (2004). EEGLAB: an open source toolbox for analysis of single-trial EEG dynamics including independent component analysis. J. Neurosci. Methods *134*, 9–21. https://doi.org/10.1016/j.jneumeth.2003.10.009.
72. Hazan, L., Zugaro, M., and Buzsáki, G. (2006). Klusters, NeuroScope, NDManager: a free software suite for neurophysiological data processing and visualization. J. Neurosci. Methods *155*, 207–216. https://doi.org/10.1016/j.jneumeth.2006.01.017.
73. Schneider, T., and Neumaier, A. (2001). Algorithm 808: ARfit—A MATLAB package for the estimation of parameters and eigenmodes of multivariate autoregressive models. ACM Trans. Math. Software *27*, 58–65. https://doi.org/10.1145/382043.382316.
74. Zhou, P., Resendez, S.L., Rodriguez-Romaguera, J., Jimenez, J.C., Neufeld, S.Q., Giovannucci, A., Friedrich, J., Pnevmatikakis, E.A., Stuber, G.D., Hen, R., et al. (2018). Efficient and accurate extraction of in vivo calcium signals from microendoscopic video data. eLife *7*, e28728. https://doi.org/10.7554/eLife.28728.
75. Liu, H., Wu, Z., Li, X., Cai, D., and Huang, T.S. (2012). Constrained nonnegative matrix factorization for image representation. IEEE Trans. Pattern Anal. Mach. Intell. *34*, 1299–1311. https://doi.org/10.1109/TPAMI.2011.217.
76. Pnevmatikakis, E.A., Soudry, D., Gao, Y., Machado, T.A., Merel, J., Pfau, D., Reardon, T., Mu, Y., Lacefield, C., Yang, W., et al. (2016). Simultaneous denoising, deconvolution, and demixing of calcium imaging data. Neuron *89*, 285–299. https://doi.org/10.1016/j.neuron.2015.11.037.
77. Hu, L., Liang, M., Mouraux, A., Wise, R.G., Hu, Y., and Iannetti, G.D. (2011). Taking into account latency, amplitude, and morphology: improved estimation of single-trial ERPs by wavelet filtering and multiple linear regression. J. Neurophysiol. *106*, 3216–3229. https://doi.org/10.1152/jn.00220.2011.
78. Hu, L., Xiao, P., Zhang, Z.G., Mouraux, A., and Iannetti, G.D. (2014). Single-trial time-frequency analysis of electrocortical signals: baseline correction and beyond. Neuroimage *84*, 876–887. https://doi.org/10.1016/j.neuroimage.2013.09.055.
79. Carmeli, C., Bonifazi, P., Robinson, H.P.C., and Small, M. (2013). Quantifying network properties in multi-electrode recordings: spatiotemporal characterization and inter-trial variation of evoked gamma oscillations in mouse somatosensory cortex in vitro. Front. Comput. Neurosci. *7*, 134. https://doi.org/10.3389/fncom.2013.00134.
80. Lasztóczi, B., and Klausberger, T. (2014). Layer-specific GABAergic control of distinct gamma oscillations in the CA1 hippocampus. Neuron *81*, 1126–1139. https://doi.org/10.1016/j.neuron.2014.01.021.
81. Mitzdorf, U. (1985). Current source-density method and application in cat cerebral cortex: investigation of evoked potentials and EEG phenomena. Physiol. Rev. *65*, 37–100. https://doi.org/10.1152/physrev.1985.65.1.37.
82. Chand, G.B., and Dhamala, M. (2014). Spectral factorization-based current source density analysis of ongoing neural oscillations. J. Neurosci. Methods *224*, 58–65. https://doi.org/10.1016/j.jneumeth.2013.12.011.
83. Yger, P., Spampinato, G.L., Esposito, E., Lefebvre, B., Deny, S., Gardella, C., Stimberg, M., Jetter, F., Zeck, G., Picaud, S., et al. (2018). A spike sorting toolbox for up to thousands of electrodes validated with ground truth recordings in vitro and in vivo. eLife *7*, e34518. https://doi.org/10.7554/eLife.34518.
84. Jun, J.J., Steinmetz, N.A., Siegle, J.H., Denman, D.J., Bauza, M., Barbarits, B., Lee, A.K., Anastassiou, C.A., Andrei, A., Aydın, Ç., et al. (2017). Fully integrated silicon probes for high-density recording of neural activity. Nature *551*, 232–236. https://doi.org/10.1038/nature24636.
85. Petersen, P.C., Siegle, J.H., Steinmetz, N.A., Mahallati, S., and Buzsáki, G. (2021). CellExplorer: A framework for visualizing and characterizing single neurons. Neuron *109*, 3594–3608.e2. https://doi.org/10.1016/j.neuron.2021.09.002.
86. Mitchell, J.F., Sundberg, K.A., and Reynolds, J.H. (2007). Differential attention-dependent response modulation across cell classes in macaque visual area V4. Neuron *55*, 131–141. https://doi.org/10.1016/j.neuron.2007.06.018.
87. Woloszyn, L., and Sheinberg, D.L. (2012). Effects of long-term visual experience on responses of distinct classes of single units in inferior temporal cortex. Neuron *74*, 193–205. https://doi.org/10.1016/j.neuron.2012.01.032.
88. Buzsáki, G., Anastassiou, C.A., and Koch, C. (2012). The origin of extracellular fields and currents–EEG, ECoG, LFP and spikes. Nat. Rev. Neurosci. *13*, 407–420. https://doi.org/10.1038/nrn3241.
89. Pesaran, B., Vinck, M., Einevoll, G.T., Sirota, A., Fries, P., Siegel, M., Truccolo, W., Schroeder, C.E., and Srinivasan, R. (2018). Investigating large-scale brain dynamics using field potential recordings: analysis and interpretation. Nat. Neurosci. *21*, 903–919. https://doi.org/10.1038/s41593-018-0171-8.

90. Schwartz, O., Pillow, J.W., Rust, N.C., and Simoncelli, E.P. (2006). Spike-triggered neural characterization. J. Vis. *6*, 484–507. https://doi.org/10.1167/6.4.13.

91. Teleńczuk, B., Dehghani, N., Le Van Quyen, M., Cash, S.S., Halgren, E., Hatsopoulos, N.G., and Destexhe, A. (2017). Local field potentials primarily reflect inhibitory neuron activity in human and monkey cortex. Sci. Rep. *7*, 40211. https://doi.org/10.1038/srep40211.

92. Ray, S., and Maunsell, J.H.R. (2011). Network rhythms influence the relationship between spike-triggered local field potential and functional connectivity. J. Neurosci. *31*, 12674–12682. https://doi.org/10.1523/JNEUROSCI.1856-11.2011.

93. Shi, K., Liu, X., Hou, L., Qiao, D., and Peng, Y. (2021). Exercise improves movement by regulating the plasticity of cortical function in hemiparkinsonian rats. Front. Aging Neurosci. *13*, 695108. https://doi.org/10.3389/fnagi.2021.695108.

STAR★METHODS

KEY RESOURCES TABLE

REAGENT or RESOURCE	SOURCE	IDENTIFIER
Bacterial and virus strains		
rAAV-CaMKIIα-hChR2(E123T/T159C)-EYFP-WPRE-hGH pA	BrainVTA	Cat# PT-0004
rAAV-CaMKIIα-eNpHR3.0-EYFP-WPRE-hGH pA	BrainVTA	Cat# PT-0008
rAAV-EF1α-DIO-hChR2(H134R)-EYFP-WPRE-hGHpA	BrainVTA	Cat# PT-0001
rAAV-EF1α-DIO-eNpHR3.0-EYFP-WPRE-hGHpA	BrainVTA	Cat# PT-0007
rAAV-CamKIIα-GCaMP6f-WPRE-hGH pA	BrainVTA	Cat# PT-0119
rAAV-EF1α-DIO-GCaMP6f-WPRE-hGH pA	BrainVTA	Cat# PT-0106
Deposited data		
Raw and analyzed data	this paper	ScienceDB Data: https://doi.org/10.57760/sciencedb.11364
Experimental models: Organisms/strains		
Mouse: PV-Cre (B6.129P2-Pvlbtm1(cre)Arbr/J)	Jackson Laboratories	RRID: IMSR_JAX:008069
Mouse: C57BL/6	Charles River	N/A
Rat: Sprague-Dawley	Charles River	N/A
Software and algorithms		
MATLAB	MathWorks	RRID: SCR_001622
EEGLAB 2019b	www.sccn.ucsd.edu/eeglab	RRID: SCR_007292
Chronux 2.12	www.chronux.org	RRID: SCR_005547
CircStat	www.github.com/circstat/circstat-matlab	N/A
phy 2.0	www.github.com/cortex-lab/phy	N/A
SpyKING-CIRCUS	www.github.com/spyking-circus	N/A
Custom analysis code	https://doi.org/10.5281/zenodo.14608070	N/A

EXPERIMENTAL MODEL AND STUDY PARTICIPANT DETAILS

In experiment 1, we collected EEG data from 95 healthy volunteers (50 females, aged 21.6 ± 1.7 years, range: 18–25 years), following an identical stimulation procedure. All subjects gave their written informed consent and were paid for their participation. All experimental procedures were approved by the ethics committee of Southwest University (experiment 1) and Institute of Psychology, Chinese Academy of Sciences (experiments 2–7) (No. H21056). In experiments 2–4, 20 adult male Sprague-Dawley rats (14 for experiments 2–3 and 6 for experiment 4), weighing between 300 and 450 g, were used for electrophysiological recordings. Rats were housed individually at a constant temperature of 23°C under a 12-h light/dark cycle with food and water available ad libitum. In experiments 5–7, male wild-type and PV-Cre mice aged 4 to 8 months (wild-type mice: C57BL/6J, Charles River, China; PV-Cre: RRID: IMSR_JAX:008069) were used. Up to four mice were group-housed at a temperature of 20°C –24°C and a humidity level of 40%–60% under a 12-h light/dark cycle with food and water available ad libitum. Following virus injection and stereotaxic surgeries, mice were individually housed. All surgical and experimental procedures strictly adhered to the guidelines for animal experimentation. Please note that data from all experiments are new, except that part of the data in experiment 1 (i.e., left hand stimulation) have previously been published.[5]

METHOD DETAILS

Surgical procedures

Before surgery (experiments 2–4), a 16-channel silicon probe (NeuroNexus, A1×16-3mm-100-703-H16_21mm) was applied with DiI solution (10 μM, diluted in ethanol) on the back of the probe shank to histologically visualize the location of the implanted probe at a later stage.[57] The surgical procedures for experiments 2–4 closely followed the details described in our previous publications,[18,58] except that a two-step strategy was adopted to reach a compromise between an optimal signal quality after the probe implantation and a better recovery from the postoperative injury.[32] In the first step, two stainless steel screws (diameter = 1 mm) were implanted into holes in the skull at 2 mm and 4 mm posterior to the posterior fonticuli, and they served as the reference and ground electrodes,

respectively. The skull area above the right S1 or M1 was exposed for the following probe implantation. A 3D-printed base plate was then fixed on the skull to protect the exposed area during the week of postoperative recovery. In the second step, the silicon probe was implanted after the rat recovered from surgery. The probe was mounted on a 3D-printed movable micro-drive and penetrated to the brain surface from the craniotomy above the exposed area. The coordinates for the probe implantation were as follows: AP: 3.0 mm, ML: 3.0 mm for M1, and AP: 0.0 mm, ML: 4.0 mm for S1 with a 10° angle from the dorsal-ventral axis to ensure the probe perpendicular to the brain surface at the target area.[59–61] The probe was lowered slowly to a depth of 1.6 mm below the brain surface. Then, the craniotomy was sealed with tissue adhesive (Kwil-sil, WPI) to protect the brain surface. Rats were allowed for an overnight recovery before recording electrophysiological data.

For virus injection in experiments 5–7, mice were anaesthetized with isoflurane and secured within a stereotaxic apparatus. In vivo delivery of recombinant adeno-associated virus (rAAVs) was performed by stereotactic injections. The injection coordinates, with reference to bregma, were as follows: left S1HL (AP: 0.58 mm; ML: -1.50 mm; DV: 0.45 mm). The delivery of rAAVs was meticulously executed, with a total volume of 0.4 μl administered over a duration of 10 min.

For *in vivo* calcium imaging (experiment 5), wild-type mice received virus encoding rAAV-CamKIIα-GCaMP6f-WPRE-hGH pA (titer: $\geq$2 x 10^{12} vg/ml), and PV-Cre mice received virus encoding rAAV-EF1α-DIO-GCaMP6f-WPRE-hGH pA (titer: $\geq$2 x 10^{12} vg/ml). Three weeks after the rAAV injection, an endoscope (GRIN lens; Part ID, 130-000151; diameter, 1.0 mm; length, 2.0 mm; Inscopix) with a custom endoscope holder was slowly implanted at the following coordinates: AP: 0.58 mm; ML: -1.50 mm; DV: 0.20 mm. Three days after endoscope implantation, mice were anesthetized with isoflurane. A baseplate (Part ID: 100-000279; Inscopix) attached to the miniature microscope was positioned above the endoscope. The focal plane (100 to 300 μm working distance) was adjusted until neuronal structures and GCaMP6f responses were clearly observed. The baseplate was then fixed in place with dental cement, and a baseplate cover (part ID: 100-000241; Inscopix) was secured to the baseplate with a set screw to protect the lens until imaging.

For optogenetic experiments (experiments 6–7), wild-type mice received virus encoding rAAV-CaMKIIα-hChR2(E123T/T159C)-EYFP-WPRE-hGH pA (titer: $\geq$2 x 10^{12} vg/ml) and rAAV-CaMKIIα-eNpHR3.0-EYFP-WPRE-hGH pA (titer: $\geq$2 x 10^{12} vg/ml), and PV-Cre mice received virus encoding rAAV-EF1α-DIO-hChR2(H134R)-EYFP-WPRE-hGHpA (titer: $\geq$2 x 10^{12} vg/ml) and rAAV-EF1α-DIO-eNpHR3.0-EYFP-WPRE-hGHpA (titer: $\geq$2 x 10^{12} vg/ml). Animals were kept at rest for 4 weeks to achieve optimal viral expression prior to experiments. An optical fiber implant (200 μm in diameter, numerical aperture [NA] of 0.37) was inserted at the position 0.3 mm above the viral injection site and secured on the skull with dental cement and a screw.

For the optetrode experiment (experiment 7), mice first received an rAAV injection into the S1HL region and were then implanted with an electrode equipped with a custom-added optical fiber (200 μm in diameter, NA of 0.37) positioned at the center and four tungsten tetrodes arranged in a square formation around the optical fiber. Tetrodes were made of 8 μm diameter tungsten wires (H-Formvar insulation with Butyral bond coat; California Fine Wire). The stripped optic fiber was lowered to a position 50 μm above the site of the viral injection and remained in place throughout the experiment. Two stainless-steel screws were implanted above the cerebellum to serve as the ground and reference. The tetrodes were implanted at a depth of 0.3 mm in the S1HL region of the brain, and the whole device was secured on the skull with dental cement.

Experimental design and sensory stimuli

Transient nociceptive laser (experiments 1, 2, 4, 5, 6, and 7) and mechanical (experiment 6), and non-nociceptive electrical (experiment 3) were applied, with one (experiments 6–7) or multiple (experiments 1–5) stimulus intensities delivered to two stimulation sides (the left and right hands or paws) in each experiment.

In experiment 1, each subject received ten laser pulses at each of the four stimulus energies (E1-E4), for a total of 40 pulses. The order of stimulus energies was pseudorandomized. The inter-stimulus interval varied randomly between 10 and 15 s with a rectangular distribution. An auditory tone delivered 3–6 s after the laser stimulation prompted the subjects to rate the intensity of the painful sensation elicited by the laser stimulus, using a numerical rating scale ranging from 0 (corresponding to "no pain") to 10 (corresponding to "pain as bad as it could be"), with 4 denoting pinprick pain threshold.[62]

In experiments 2–5, each subject received a total of 60 stimuli, with 15 stimuli delivered per intensity and side. In experiments 6–7, for each type of mice and each optogenetic virus, a total of 80 stimuli were delivered, with 20 stimuli per side and optogenetic condition. The inter-stimulus interval between two consecutive stimuli was >30 s.

Radiant-heat nociceptive laser stimuli were generated by an infrared neodymium yttrium aluminum perovskite (Nd:YAP) laser with a wavelength of 1.34 μm (Electronical Engineering, Italy), which activates directly cutaneous nociceptive terminals in the most superficial skin layers.[63,64] An optic fiber transmitted the laser beam, whose diameter was set at approximately 7 mm (~38 mm^2) in the human experiment and 5 mm (~20 mm^2) in rodent experiments by focusing lenses. The laser pulses (duration = 4 ms) were delivered to the skin of either the left or right hand/paw. To avoid nociceptor fatigue or sensitization, the target of the laser beam was altered after each stimulus.[65] In experiment 1 (involving humans), we used four stimulus energies (E1: 2.5 J; E2: 3 J; E3: 3.5 J; E4: 4 J). In experiments 2 and 4 (involving rats), high and low stimulus energies were set to 3.5 J and 3.0 J, respectively. In experiment 5 (involving mice), high and low stimulus energies were set to 2.0 J and 1.5 J, respectively. For experiments 6–7 (involving mice), a fixed stimulus energy of 1.5 J was used.

Non-nociceptive electrical stimuli were constant current square-wave electrical pulses generated by a multichannel electrical stimulator (SXC-4A, Sanxia Technique Inc., China).[66] Electrical pulses (duration = 1 ms) were delivered through a pair of moveable

electrodes (inter-electrode distance = 1.5 mm) that were contacted with either the left or right forepaw of rats (experiment 3). High and low stimulus intensities were set to 1 mA and 0.75 mA, respectively.

A series of von Frey filaments (bending forces: 0.02, 0.04, 0.07, 0.16, 0.4, 0.6, 1, and 2 g) were employed to assess the mechanical pain threshold in mice (experiment 6).[67] The minimal force filament that elicited an obvious paw withdrawal or escape response in at least five out of ten stimuli was defined as the mechanical pain threshold. To ensure accurate measurements, von Frey filaments were applied with an interval of at least 5 s after the mice had returned to their initial resting state following the previous stimulus.

Data collection

Human electrophysiological recording (experiment 1)

EEG data were recorded using 64 AgCl electrodes positioned according to the extended 10–20 system (Brain Products GmbH, Munich, Germany; pass band: 0.01–100 Hz; sampling rate: 1,000 Hz). The nose was used as the reference, and impedances were kept lower than 10 kΩ in all electrodes. To monitor ocular movements and eye blinks, electro-oculographic signals were simultaneously recorded from two bipolar electrodes: one pair placed over the upper and lower eyelids of the left eye, the other pair placed 1 cm lateral to the outer corner of the left and right orbits.

Rat electrophysiological recording (experiments 2–4)

Electrophysiological signals were recorded at a sampling rate of 40,000 Hz using a Multichannel Acquisition Processor (OmniPlex, Plexon, USA). Before the recording session, animals were placed for 1 h in a plastic chamber (30 × 30 × 30 cm^3) to familiarize them with the recording environment. During the recording session, animals were allowed to move freely in the chamber. Laser or electrical stimuli were delivered to the plantar surface of either left or right forepaw through gaps in the chamber floor when the animal was spontaneously still. To avoid the activation of the auditory system by laser-generated ultrasounds, white noise (70 dB SPL) was continuously played throughout the recording session, which allowed for a selective recording of brain responses associated with the activation of the nociceptive system.[65]

Animals' behaviors were video-recorded throughout the experiment, and behavioral scores were assigned based on their movements after each stimulus, according to previously defined criteria.[68] Specifically, stimulus-evoked behaviors were categorized into 5 types: no movement (score = 0), head turning (including shaking or elevating the head; score = 1), flinching (characterized by a small abrupt body jerking movement; score = 2), withdrawal (denoting paw retraction from the stimulus; score = 3), and licking and whole-body movement (score = 4).

Calcium imaging (experiment 5)

Prior to data collection, mice underwent a 2-day habituation period, during which they were introduced to the microscope attachment for 30 min each day within an acrylic cage (7.5 × 7.5 × 15 cm^3) with a fine mesh grid floor. Then, a head-attached microscope (Inscopix; LED power: 0.6 to 1.0 mW; camera resolution: 1,440 × 1,080 pixels) was employed for calcium imaging in freely-moving mice. The imaging was conducted at a frame rate of 20 Hz using nVista HD software (Inscopix). The synchronization of laser triggering with calcium imaging was achieved by connecting the laser trigger to the trigger-out signal of nVista HD.[69] Before each imaging session, the baseplate cover on the previously implanted baseplate was removed, and the microscope was securely attached. The imaging field of view covered an area of approximately 900 × 600 μm^2 with a resolution of 0.65 μm/pixel. The imaging depth was adjusted by focusing the microscope until clear signals from cells, appearing as bright spots in the images, were observed. The focal plane was set between 250 and 500 μm below the lens. Mice's behaviors were concurrently recorded using the same methodologies as in experiment 2.

Optogenetic stimulation and electrophysiological recording (experiments 6–7)

Before testing and data collection, mice were habituated to a small acrylic cage (7.5 × 7.5 × 15 cm^3) for at least 30 min. Optogenetic stimulation was achieved using an LED module (473 nm and 590 nm) mounted on a dual LED commutator connected to an optogenetic controller (PlexBright, Plexon Inc., Dallas, TX). For optogenetic activation of pyramidal neurons, a train of photostimuli consisted of blue light pulses (473 nm, 10 Hz, and 3 ms duration for each pulse) was delivered for 10 s with the illumination intensity of 5 mW.[45] For optogenetic activation of PV interneurons, a train of photostimuli consisted of blue light pulses (473 nm, 40 Hz, and 1 ms duration for each pulse) was delivered for 10 s with the illumination intensity of 5 mW.[45] For optogenetic inhibition of both neurons, photostimuli consisted of continuous yellow light (590 nm) with the illumination intensity of 30 mW were delivered for 10 s.[70] Between the control and optogenetic tests, there was a 30-min interval for rest. Nociceptive laser and mechanical stimuli were delivered when the LED light was on in the optogenetic test. Electrophysiological signals were recorded using the same procedures as in experiment 2, except that optetrodes were used for data collection and that nociceptive laser stimuli were delivered to the left or right hindpaw of mice.

Histology and immunohistochemistry

After the recording session, rats and mice were anesthetized with 1% sodium pentobarbital (0.1g/kg i.p.) and perfused intracardially with 0.9% saline followed by 4% paraformaldehyde (PFA, in 0.1 M phosphate buffer, pH 7.4). The isolated brains were post-fixed with 4% PFA for 12 h, and cryoprotected in 20% and 30% sucrose solutions in turn. The fixed brains were cut into 50-μm thick slices to identify probe tracks marked by DiI and to detect virus expression through fluorescence.

For Nissl staining, free-floating brain sections were first washed in the phosphate-buffered saline (PBS) containing 0.1% triton-100 for 10 min and then rinsed three times for 5 min each in PBS. The sections were incubated with the NeuroTrace Nissl stain (1:100 diluted in PBS, N21480, Thermo Fisher) at room temperature for 20 min. Subsequently, the stain was removed, and the sections

were washed three times for 5 min each in PBS. The brain slices were photographed by a fluorescence microscope (Leica DMI 4000B, Wetzlar, Germany).

QUANTIFICATION AND STATISTICAL ANALYSIS

Data preprocessing

In experiment 1, EEG data were processed using EEGLAB,[71] an open source toolbox running in the MATLAB environment, and in-house MATLAB functions. Continuous EEG data were band-pass filtered between 1 and 100 Hz. EEG epochs were extracted using a window analysis time of 1500 ms (500 ms pre-stimulus and 1000 ms post-stimulus) and baseline corrected in the time domain using the pre-stimulus interval. Trials contaminated by eye-blinks and movements were corrected using an Independent Component Analysis algorithm (runica), and the IClabel algorithm was adopted to automatically identify and remove any ICs unrelated to brain.[71]

In experiments 2, 3, 4, and 7, electrophysiological data were preprocessed using NDManager[72] and in-house MATLAB functions. To extract stimulus-evoked responses, electrophysiological data were down-sampled to 1000 Hz, bandpass filtered between 1 and 100 Hz, and notch filtered between 48 and 52 Hz. Peri-stimulus epochs were extracted from continuous data using a time window of 1500 ms (-500 ms to +1000 ms relative to stimulus onset), and were baseline corrected using the pre-stimulus interval. Epochs contaminated by gross artifacts were discarded. Moreover, ARfitStudio, an extension in EEGLAB[73] to interactively eliminate the short-burst (5 to 10 ms) artifacts, was adopted to eliminate the electrical-induced artifacts in LFP epochs. Specifically, ArfitStudio trained an autoregressive model from the signals before electrical stimuli (~10 to 20 ms) and made predictions of the signals after electrical stimuli (0 to 5 ms) to remove the electrical-induced artifacts (Figure S1C).

In experiments 2–3, to standardize depth coordinates of S1 across rats, we aligned depth profiles using electrophysiological landmarks derived from CSD estimation. Since landmarks of laminas responding to tactile stimuli have been well investigated,[34] depth profiles from different rats were aligned according to these landmarks and the distance between adjacent Layers was "warped" (either extended or stretched) using linear interpolation.[32,34] Specifically, the landmarks were obtained from CSD estimation of LFP responses evoked by electrical stimuli delivered to the left forepaw (i.e., contralateral to the right S1 with the implanted probe). The obtained landmarks featured with two sinks that occurred in Layer IV and Layer Vb, and three sources in Layer I, Layer Va, and Layer VI. The borders between adjacent sinks and sources were used to estimate the thickness of the corresponding layer for each rat. According to the layer thickness, signals at different depth were "warped" based on the predetermined distances (100 μm, 400 μm, 300 μm, 200 μm, 300 μm, and 300 μm for Layers I, II/III, IV, Va, Vb, and VI, respectively) to ensure that the number of electrodes within the same layer was identical for different rats (Figure S1E).

In experiment 5, calcium imaging data were preprocessed using the Inscopix Data Processing toolbox (Inscopix), including the following steps: spatial and temporal downsampling of the data; filtering of the images; calculating the mean image of the filtered video; motion correction analysis based on the mean image.[74] Next, the average fluorescence intensity of each pixel during the recording period was calculated as F0. The change in fluorescence intensity at time (t) was expressed as (F(t) – F0)/F0 or ΔF/F0. Subsequently, the CNMFe algorithm was applied to the spatiotemporal data matrix of ΔF/F0 to identify active neurons for further analyses.[75] The neurons were arranged based on the timing of events, resulting in a ΔF/F0 change graph of neurons in response to the events. The fast optimal optical spike inference (foopsi) algorithm was adopted for the deconvolution of fluorescence signals to eliminate noise.[76]

Time-domain and time-frequency domain analyses

In experiments 1–4, single-trial EEG/LFP responses were averaged across trials for each subject and experimental condition in the time domain. For human experiment, the EEG responses were re-referenced to Fz electrode to optimally extract the earliest part of the laser-evoked brain responses, i.e., the N1 wave, at ~160 ms relative to stimulus onset.[5,77] For animal experiments, the amplitude of the dominant negative peak (~20 ms and ~150 ms for electrical and laser stimuli, respectively) was measured from average LFP waveforms at different depths. Single-subject average waveforms were subsequently averaged to obtain the group-level EEG/LFP waveforms.

Time-frequency representations of single-trial EEG/LFP responses were calculated using a windowed Fourier transform with a fixed Hanning window (200 ms for laser stimuli and 100 ms for electrical stimuli due to their difference in response duration). A complex time-frequency spectrum F(t, f) was estimated for each trial from -500 to 1000 ms (in steps of 2 ms) in latency and from 1 to 100 Hz (in steps of 1 Hz) in frequency. The resulting spectrogram $P(t, f)=|F(t, f)|^2$ represents the power spectral density as a joint function of time and frequency at each time-frequency point. Single-trial spectrograms were baseline corrected by subtracting the mean signals within the pre-stimulus interval for each frequency (-400 to -100 ms relative to stimulus onset),[78] and then averaged across trials for each subject and experimental condition. To isolate GBO responses, we calculated the time course of GBO amplitude by averaging spectrograms across gamma frequencies from 60 to 90 Hz. The amplitude of the dominant peak in GBO time courses was measured by calculating the maximal power within a pre-defined interval (0–100 ms and 100–300 ms for electrical and laser stimuli, respectively) at different depths.

Subsequently, we performed a point-by-point statistical analysis to identify spatial layers and time intervals in which low-frequency ERP responses or high-frequency GBO responses were different between experimental conditions. Specifically, for each spatiotemporal point, we performed a two-way repeated-measures ANOVA to assess the possible effects of 'Intensity' (two levels: high and

low), 'Side' (two levels: left and right), and their interaction. To account for multiple comparisons, the significance level (expressed as *p* value) was corrected using a false discovery rate (FDR) procedure. Please note that electrophysiological signals in experiment 7 were analyzed using the same procedures in the time and time-frequency domains as in experiment 2. Please also note that to evaluate the dependence of brain responses on pain intensity, we sorted trials according to nocifensive behaviors and median-split them into high rating trials and low rating trials for each stimulation side for statistical analyses. As a result, the factor "Intensity" means ratings of nocifensive behaviors or simply pain intensity.

In experiment 5, after preprocessing, the calcium imaging data were normalized to express as *Z* scores, and then baseline corrected by subtracting the mean signals within the pre-stimuli intervals (-5 to 0 s relative to stimulus onset). Then, the data was averaged within a 5-s window after the onset of each trial under different experimental conditions. This process resulted in the response profile of individual neurons for each experimental condition.

Linear mixed model (LMM) analysis

In experiment 1, to examine the relationship between (1) stimulus intensity and neural responses as well as (2) subjective ratings and neural responses, we performed LMM to single-trial time-frequency representations that capture the intraindividual variability.[27] LMM analysis was also applied to assess whether the relationship between pain intensity and neural responses persisted independent of stimulus intensity by normalizing pain ratings and neural responses as *Z* scores for each stimulus intensity. Specifically, we fit the LMM for pain score or stimulus intensity (y), with the same fixed-effects GBOs (x), and correlated random effect for intercept and GBOs grouped by the subject (sub). The Wilkinson's notation of the mixed model formulation is y∼1+x+(1+x|sub). LMM was performed for each data point of the baseline corrected single-trial time-frequency representations, yielding the relationship between neural responses and stimulus intensity/pain intensity as a function of time and frequency. FDR correction was applied to account for multiple comparisons. Please note that trials with stimuli delivered to the left and right hands were merged during the LMM analyses since GBOs elicited by nociceptive stimuli were not modulated by stimulation side and showed a centrally distributed scalp topography (Figure 2C). To statistically compare the onset latencies of the three LMM effects, we re-ran the LMMs on subsampled datasets (randomly selecting 80% of subjects) for 20 times and then extracted the corresponding onset latencies. Onset latency was defined as the earliest time point with significant *p* values in the temporal profile of the LMM results averaged within the 50–100 Hz frequency range.

To reveal the dose-response curve between pain intensity/stimulus intensity and GBO amplitudes, we sorted the trials according to pain ratings or stimulus intensities by uniformly incremental levels (i.e., for pain intensity, sorted by pain ratings from 4 to 10 in steps of 1; for stimulus intensity, sorted with fixed four levels: 2.5J, 3J, 3.5J, 4J). The GBO amplitudes or the normalized GBO amplitudes within the significant pixels (above 50 Hz after the stimulus onset) extracted from LMMs were averaged for each level and then fitted with a linear function. Given that the instruction that 4 denoted pinprick pain threshold might have been confusing as all ratings between 0 and 3 meant no pain, trials with pain ratings lower than 4, i.e., below the pinprick pain threshold, were excluded when assessing the relationship between pain intensity and GBO amplitudes.

Current source density (CSD) estimation

To demonstrate the spatiotemporal distributions of stimulus-evoked electrophysiological responses in experiments 2–3, we adopted the CSD estimation method that can be applied to the recordings at equidistant, linearly positioned electrode contacts vertically penetrating the cortical layers.[79] Specifically, CSD was calculated on across-trial averaged LFP responses for each experimental condition by estimating the second spatial derivative of LFP responses using the following equation:

$$CSD_{n,t} \approx -\sigma_z \frac{LFP_{n-1,t} - 2 * LFP_{n,t} + LFP_{n+1,t}}{\Delta z^2}$$

where $LFP_{n,t}$ is the potential sampled on the silicon probe contact *n* at time *t*, $LFP_{n-1,t}$ and $LFP_{n+1,t}$ represent the sampled potentials on the neighboring contacts at time *t*. Δz is the spacing between adjacent silicon probe contacts. σ_z is the z-directional component of tissue conductivity.[80,81]

Unlike the low-frequency ERP responses, high-frequency GBO responses could be non-phase-locked to the onset of sensory stimuli.[6] The non-phase-locked responses would be largely canceled out by time-domain across-trial averaging, thus suppressing the spatiotemporal variations of the responses.[82] For this reason, the CSD of GBO responses was calculated on the time course of GBO amplitude that was derived from the time-frequency analysis.

To isolate significant spatiotemporal variations from background fluctuation, CSD estimates were first baseline corrected by subtracting the mean signals within the pre-stimulus intervals for each probe contact (-100 to 0 ms relative to stimulus onset). Then, CSD estimates across all experimental conditions for each sensory modality were thresholded using a cut-off at three standard deviations from the mean for each contact. Spatiotemporal regions with CSD estimates above (source) or below (sink) three standard deviations from the mean were identified and marked with dashed circles (Figures S2C, S2D, S4C, and S4D).

Spike detection and classification

The raw electrophysiological data in experiments 2–3 were high-pass filtered at 200 Hz, and spikes were sorted using the open-source algorithm SpyKING CIRCUS (www.github.com/spyking-circus), a method that relies on density-based clustering and

template matching to assign spike clusters to individual contacts in electrode arrays without cluster overlay.[83] The templates of spike clusters were created by phy 2.0 (www.github.com/cortex-lab/phy), which provides an interactive visualization and manual spike sorting of large-scale electrophysiological data.[84] Subsequently, spike units were classified using CellExplorer,[85] and were generated from putative pyramidal neurons or interneurons based on the duration of the action potential, which is defined as the latency difference between the trough and the peak of the waveform. Based on the bimodal distribution of the durations of all recorded spikes, a data-driven approach was adopted to determine the threshold to separate interneurons from pyramidal neurons (i.e., the pit between the two peaks of the distribution),[18,86,87] which was 400 μs in the present study (Figure S1F).

To calculate spike density functions for intuitively illustrating the modulation of spike firing by sensory stimuli, the electrophysiological data were segmented using a window analysis time of 1500 ms (-500 ms to +1000 ms with respect to stimulus onset). For each trial, the spike firing rate was binned using a 100-ms window and normalized to the baseline using the Z score (i.e., dividing the baseline-subtracted value by the standard deviation within the pre-stimulus interval). The obtained spike density functions were then averaged across trials for each neuron to provide a general presentation of response patterns for different sensory modalities (Figure S1G).

Identification of functionally differentiated neurons

To identify neurons with distinct functions in encoding stimulus attributes, the singular values of the binned spike data (see spike detection and classification) within the predefined time intervals (0–50 ms and 0–300 ms for electrical and laser stimuli, respectively) were calculated as a summative parameter of spike firing at the single-trial level. For each sensory modality, the singular values were submitted to the two-way repeated-measures ANOVA to assess whether the spike firing would be affected by the factor 'Intensity', 'Side', or their interaction. According to the statistical results, neurons were divided into five distinct groups: neurons significantly modulated ($p < 0.05$) by (1) 'Intensity' only, (2) 'Side' only, (3) 'Intensity' and 'Side', (4) 'Intensity' × 'Side' interaction, and (5) none of the previous (Figures S3A–S3C and S5A–S5C). Chi-squared tests were performed to compare the proportion of neurons with distinct functions between pyramidal neurons and interneurons within the same modality.

Likewise, neurons identified in the calcium imaging data in experiment 5 were categorized using the same procedures as described above. Normalized calcium signals were obtained by calculating the mean values within the predefined time interval ranging from 0 to 5 s and then compared using the same statistical procedures employed for analyzing the electrophysiological data.

Spike-triggered field potentials for functionally differentiated neurons

Since strong correlations were observed between LFPs and nearby intracellular spike activities,[88,89] it would be interesting to assess the relationship between different LFP features and functionally differentiated neurons. The spike-field synchronization was evaluated by estimating the spike-triggered average LFPs (STA) using the following equation:

$$STA(t) = \frac{1}{N}\sum_{k=1}^{N} LFP(t - t_k)$$

where N is the amount of spike firing times in the given intervals (0–50 ms and 0–300 ms for electrical and laser stimuli, respectively), and t_k is the onset of spike time of the triggering unit. STA could demonstrate the contribution of a specific spike unit to stimulus-evoked LFPs.[90,91]

STA estimates were obtained for pyramidal neurons and interneurons with distinct functions (i.e., those modulated by (1) 'Intensity' only, (2) 'Side' only, (3) 'Intensity' and 'Side'). To avoid variations, the spike units with less spike firing times (less than 25) were excluded.[92] Subsequently, we calculated the amplitude of the negative peak in STA estimates surrounding the onset of spike time and the phase of the STA estimates at the onset of spike time by computing the instantaneous phase using the Hilbert transformation.[91,93] Non-parametric Scheirer–Ray–Hare tests were then performed to assess whether the peak amplitude would be modulated by the factor 'neuron type' (two levels: pyramidal neurons and interneurons), 'functional group' (three levels: affected by 'Intensity', 'Side', and 'Both'), or their interaction. Post hoc tests were performed using pairwise Mann-Whitney tests or t-tests with the Sidak correction. Moreover, the Rayleigh Z test in the CircStat toolbox was performed to determine whether local field potentials are phase-locked to spike populations (Figures 4K, 5K, S3G, and S5G).

Statistical analysis

For behavior scores and neural responses in experiments 1–5, we performed a two-way repeated-measures ANOVA to assess the effects of 'Intensity' (four levels: E1, E2, E3, and E4 in experiment 1; two levels: high and low in experiments 2–5), 'Side' (two levels: left and right), and their interaction. For behavior data and neural responses in experiments 6–7, we performed a two-way repeated-measures ANOVA to assess the effects of 'Optogenetic condition' (two levels: control and ChR2/NpHR), 'Side' (two levels: left and right), and their interaction, for each type of mice and each optogenetic virus. Post hoc comparisons were performed using paired-sample t tests with Bonferroni correction.